Remote Sensing of Environment 316 (2025) 114486

Contents lists available at ScienceDirect

Remote Sensing of Environment

journal homepage: www.elsevier.com/locate/rse

Exploring the potential of SAR and terrestrial and airborne LiDAR in predicting forest floor spectral properties in temperate and boreal forests

Audrey Mercier [a,*], Mari Myllymäki [b], Aarne Hovi [a], Daniel Schraik [a,b], Miina Rautiainen [a]

[a] School of Engineering, Aalto University, Espoo, Finland
[b] Natural Resources Institute Finland (Luke), Latokartanonkaari 9, Helsinki, 00790, Finland

ARTICLE INFO

Edited by Marie Weiss

Keywords:
Forest structure
Hyperspectral
LiDAR
Terrestrial laser scanning
Airborne laser scanning
Synthetic aperture radar

ABSTRACT

Forest floor vegetation plays a crucial role in ecosystem processes of temperate and boreal forests. Remote sensing offers a valuable tool to characterize the forest floor through reflectance spectra. While passive optical airborne and satellite data have been used to map spectral properties of forest understory, these sensors are limited by cloud cover, especially in high latitudes. To date, LiDAR and SAR have not been explored for this application even though their data are less dependent on illumination conditions and provide information on tree canopy structure and tree distribution which is connected to forest floor properties. We investigated active remote sensing techniques to establish links between forest structure and spectral properties of forest floor across European temperate, hemiboreal and boreal forest ecosystems. First, in the exploratory part, the research question was : Which forest structure metrics are connected to the spectral properties of the forest floor? Next, our predictive part focused on: What is the potential of (1) terrestrial laser scanning (TLS) data, (2) airborne laser scanning data, (3) satellite-borne SAR data, and (4) these data sources combined to predict forest floor spectral properties? Our results revealed that nine forest structure metrics were potentially associated with forest floor reflectance. We identified TLS-derived clumping index and SAR-derived VV backscatter coefficient and VH/VV ratio as significantly connected to forest floor reflectance in certain Sentinel-2 spectral bands. Overall, the active remote sensors achieved the best predictions for forest floor reflectance in red-edge, near-infrared and shortwave infrared regions. Using data from all three sensors together to predict the forest floor spectra yielded better results than using any of the sensors alone. When data from a single sensor were used, the highest prediction accuracies for forest floor reflectance in the red-edge and near-infrared regions were achieved with SAR data, and in the shortwave infrared region with either SAR or TLS data. In the future, the accuracy of predicting forest floor characteristics in temperate and boreal forests could benefit from a synergy of passive and active technologies.

1. Introduction

Information on forest floor characteristics is important for a comprehensive understanding of forest ecosystems and their response to climate change. Forest floor vegetation plays a key role in the photosynthetic and nutrient cycles of a forest ecosystem (Goulden and Crill, 1997; Morén and Lindroth, 2000; Kolari et al., 2006; Rantala et al., 2011), controls water quality and contributes to the biodiversity of a forest (Rantala et al., 2011). Furthermore, changes in the understory of temperate and boreal forests observed over recent decades appear to be correlated with climate change (Herk et al., 2002; Hedwall et al., 2021; Braziunas et al., 2024), forest management practices (Hedwall et al., 2021) and forest fragmentation (De Frenne, 2023; Koelemeijer et al., 2023). There is also evidence that understory vegetation responds substantially to forest disturbances (De Frenne et al., 2021), and thus, more attention should be directed to developing methods for monitoring forest floor characteristics.

Repetitive and large scale surveys of forest floor vegetation are extremely laborious, and hence, remote sensing offers a valuable tool to monitor forest floor characteristics from local to regional spatial scales. Studies based on spectrometer measurements have previously demonstrated the potential of *in situ* spectral data to discriminate mosses (Hallik et al., 2009), lichens (Kuusinen et al., 2020, 2023), berries (Forsström et al., 2019), and common understory types (Rautiainen et al., 2011) in boreal forests. Temporal variations in the understory during the peak growing period (e.g., phenological

* Corresponding author.
E-mail address: audrey.mercier@aalto.fi (A. Mercier).

https://doi.org/10.1016/j.rse.2024.114486
Received 11 March 2024; Received in revised form 24 July 2024; Accepted 21 October 2024
Available online 3 November 2024

changes in chlorophyll content and plant structure) also affect its spectral properties in boreal (Rautiainen et al., 2011) and hemiboreal forests (Nikopensius et al., 2015). Despite the potential of spectral data shown by *in situ* studies, monitoring understory characteristics at larger spatial scales using airborne or spaceborne spectral data is challenging because most pixels in the remotely sensed data are composed of a mix of signals from the forest floor and tree layer (Rautiainen and Stenberg, 2005; Eriksson et al., 2006). This challenge has been overcome by using multiangular optical satellite data to separate understory and canopy contributions (Canisius and Chen, 2007; Pisek et al., 2012, 2021). However, multiangular images are not readily available at higher spatial resolutions, and thus, alternative methods that do not require more than one viewing angle have been developed for local forest floor mapping applications. For example, Markiet and Mõttus (2020) demonstrated the retrieval of forest floor spectral properties from single-view passive optical remote sensing data by modeling the remote sensing signal with a physical model, and then solving for forest floor reflectance. Hovi et al. (2023) used a similar approach (although a different model), and further used active remote sensing data (airborne LiDAR) to parameterize the tree canopy structure in a forest reflectance model.

The above mentioned studies have demonstrated the potential of passive optical remote sensing data for mapping forest floor spectral properties, which in turn are linked with biophysical characteristics of the forest floor. Retrieval of forest floor characteristics from active remote sensing data exclusively, such as SAR and LiDAR data, has not been yet attempted. We hypothesize that development of such methods should be feasible because ecological studies have shown that there is a clear connection between forest overstory and understory structure and composition in temperate and boreal forests (Messier et al., 1999; Barbier et al., 2008; Majasalmi and Rautiainen, 2020). In addition, some of the limitations of passive optical data, such as the uncertainty in retrieving forest floor spectral properties in dense forests (Hovi et al., 2023) and their strong dependence on illumination conditions, could be overcome by active remote sensing data.

Forest structure metrics are increasingly being derived from active remote sensors such as terrestrial laser scanning (TLS) (Schraik et al., 2023; Acebes et al., 2021; Di Stefano et al., 2021; Guo et al., 2020), airborne laser scanning (ALS) (Holzwarth et al., 2020; Acebes et al., 2021; Di Stefano et al., 2021; Guo et al., 2020) and synthetic-aperture radar (SAR) (Holzwarth et al., 2020; Bruggisser et al., 2021; Rosenqvist et al., 2021). TLS is the most accurate sensor for representing 3D forest structure at the local scale (Guo et al., 2020) and is also the only one able to provide detailed characterization of vegetation layers under the tree canopy (Disney, 2019). Thus, TLS data has the potential to deepen our understanding of the relationships between forest structure and forest floor characteristics. However, TLS is limited to the local scale, whereas ALS allows the acquisition of point clouds on a regional scale (Di Stefano et al., 2021), hence it has been widely used to derive forest structure metrics to approximate light conditions in forests (Zellweger et al., 2019) and establish links between forest structure and biodiversity (Acebes et al., 2021). SAR satellite data, on the other hand, is the most suitable to cover large areas frequently, the SAR signal is influenced by forest structure and has been widely used to predict forest aboveground biomass (Santoro et al., 2019; Mulatu et al., 2019; Holzwarth et al., 2020; Rosenqvist et al., 2021) with a positive correlation between biomass and backscatter coefficient. However, SAR signal saturation is known to occur at high leaf area index (LAI) values (Joshi et al., 2017). Nevertheless, SAR data could open opportunities for monitoring changes in understory vegetation driven by forest structural changes.

Metrics describing the three-dimensional forest canopy structure, derived from TLS, ALS and SAR data, allow us to explore new types of tree canopy characteristics compared to traditional forest inventory variables. Several studies have established links between tree canopy characteristics and the spectral properties of understory. For example, Hallik et al. (2009) have demonstrated that canopy density impacts the spectral properties of mosses in hemiboreal forests, and Rautiainen and Heiskanen (2013) have shown relationships between forest floor spectra and light availability and canopy cover in boreal forests. Finally, Forsström et al. (2023) have found that forest floor reflectance spectra and fractional cover (for vascular plants, non-vascular plants, and intact plant litter) are linked to the light availability at the forest floor, especially in visible and shortwave infrared regions (SWIR).

This paper reports a pilot study on using active remote sensing technologies (TLS, ALS, SAR) to establish links between forest structure and spectral properties of forest floor across European temperate, hemiboreal and boreal forest ecosystems. The study builds on the previously reported ecological interconnections between forest floor characteristics, light availability and forest structure. We focus on the reflectance spectrum of a forest floor because it is a versatile indicator of the health and phenological status of forest floor vegetation and also needed in climate models. Forest floor (or understory) spectral properties can be directly applied in, for example, monitoring post-disturbance recovery of forest ecosystems (Hovi et al., 2023), as input to digital twins of forests (Mõttus et al., 2021) or land surface models that form a part of climate models (Fisher and Koven, 2020) adapting to end-users' requirements by enabling them to formalize their own conceptualization of the forest floor ecosystem. In addition, focusing on continuous data (spectra) rather than discrete classes preserves the natural gradient present in vegetation, providing a more realistic representation of reality and better meeting ecosystem monitoring requirements (Rocchini et al., 2013).

In the first, exploratory part of the study, we focused on understanding which forest structure metrics are connected to the spectral properties of the forest floor. In the second, predictive part, we assessed the potential of (1) TLS data, (2) ALS data, (3) satellite-borne SAR data, and (4) all these data sources combined in predicting forest floor spectral properties during the growing season. The novelty of this study is the use of active remote sensors to predict the spectral properties of the forest floor.

2. Study area and data

2.1. Study areas

The data were acquired from four study areas in forests varying in climate, structure and compositional types located in Bílý Kříž and Lanžhot in the Czech Republic, Järvselja in Estonia, and Hyytiälä in Finland (Fig. 1, Table 1). The Bílý Kříž site (49° 30′N, 18° 32′E) comprises four stands located in a temperate mountain forest dominated by conifers. The forest floor was composed of low-growing dwarf shrubs, graminoids, moss, and needle litter. The Lanžhot site (48° 41′N, 16° 57′E) includes nine stands in a temperate floodplain forest dominated by deciduous trees. The forest floor was composed mainly of leaf litter, and herbaceous plants in stands with open tree canopy. The Järvselja site (58° 17′N,27° 19′E), located in a hemiboreal forest, comprised nine stands dominated by deciduous trees or conifers. The forest floor was composed of tall herbaceous plants. In less fertile stands, dwarf shrubs and mosses were also present. Intact plant litter was mainly found in stands not covered by green vegetation. The Hyytiälä site (61° 51′N, 24° 18′E), located in a boreal forest, included 15 stands, the majority dominated by conifers and the remainder by deciduous trees. The forest floor was composed of graminoids, mosses, dwarf shrubs, lichens, and plant litter. For more information on the structure and plant functional type composition of the study areas, please see Hovi et al. (2022) and Forsström et al. (2023).

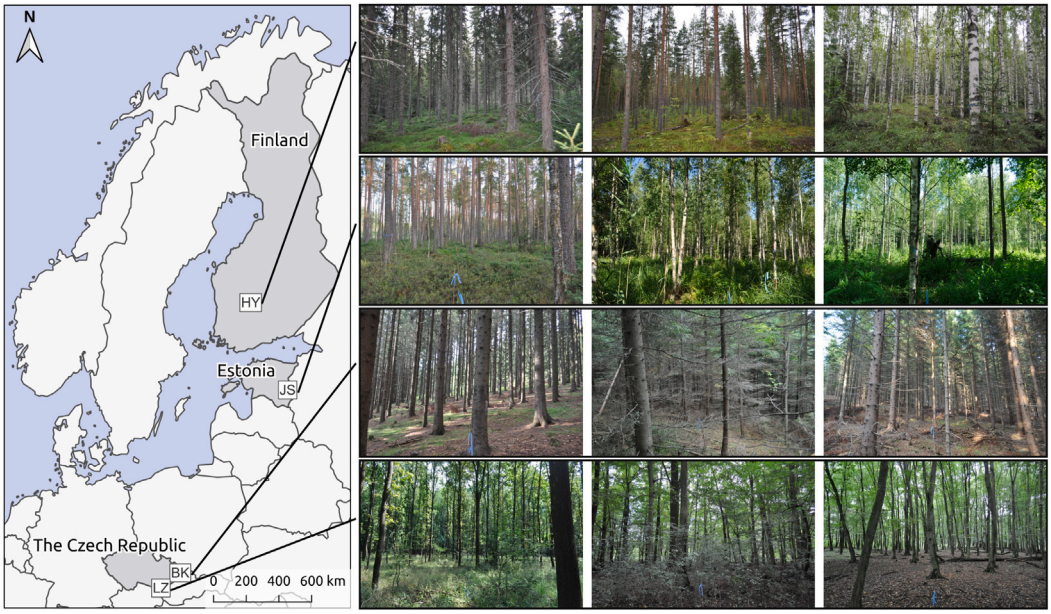

Fig. 1. Location of the four study areas. HY = Hyytiälä, JS = Järvselja, BK = Bílý Kříž, LZ = Lanžhot. The photographs show the forest environment of the study areas. Photographs adapted from Hovi et al. (2022) License: CC BY 4.0.

2.2. Forest floor spectra

We used forest floor reflectance spectra acquired during the growing season in 2019 in Hyytiälä, Bílý Kříž and Lanžhot, and 2020 in Järvselja (Fig. 2) (Forsström et al., 2023). These datasets provide Hemispherical-Conical Reflectance Factor (HCRF) values at wavelengths from 350 to 2500 nm acquired *in situ* with an ASD FieldSpec4 standard-res spectrometer (serial number 18 456) and bare fiber-optic cable as detector. HCRF values are typically between 0 and 1, in our data, they ranged from 0 to 0.63 (Appendix A). For each stand, spectra were measured at 15 positions along an 11-m-long East-West oriented transect (Fig. 3). White reference measurement was conducted at every third measurement position, and dark current once per transect. Measurements were done in nadir view and under diffuse illumination conditions. The HCRF was computed per wavelength using the following equation:

$$\mathrm{HCRF}(\lambda) = \frac{\mathrm{DN}_{\mathrm{target}}(\lambda) - \mathrm{DN}_{\mathrm{dc}}(\lambda)}{\mathrm{DN}_{\mathrm{wr}}(\lambda) - \mathrm{DN}_{\mathrm{dc}}(\lambda)} * \mathrm{R}_{\mathrm{ref}}(\lambda)$$

where DNs are the wavelength dependent (λ) signal values from target (target), white reference panel (wr) and dark current (dc) measurements, respectively. R_{ref} is the reflectance of the white reference panel (a Spectralon® panel with 99% nominal reflectance). Data collection and processing steps have been detailed in Forsström et al. (2023).

The spectra were smoothed using a Savitzky-Golay filter from the gsignal R package (Geert et al., 2021). We used a polynomial order of 2 and a 15 nm window for wavelengths equal or below 1000 nm and a 39 nm window for wavelengths above 1000 nm. We then calculated an average HCRF spectrum for each stand by averaging the 15 measurements. Finally, we removed the HCRF values corresponding to wavelengths with noisy spectra due to atmospheric attenuation (from 1336 to 1504 nm, 1781 to 2094 nm and 2316 to 2500 nm). Appendix A shows the forest floor spectra for all study stands.

2.3. Forest structure metrics

TLS, ALS and SAR data were used to describe horizontal and vertical forest structure (Fig. 3). Thirteen forest structure metrics, listed in Table 2, were defined based on previous work focusing on forest ecology (Acebes et al., 2021; Bruggisser et al., 2021) and derived for the 37 stands on the four study areas. Our methodology prioritized aligning single-date acquisitions (i.e. TLS and ALS) with the dates of forest floor reflectance spectra acquisition and averaging SAR multitemporal data over the peak growing season (Fig. 2). Averaging SAR data reduces the impact of short-term variability and noise.

2.3.1. Terrestrial laser scanning

We acquired TLS scans in all plots in July and September 2019 in Hyytiälä, Bílý Kříž and Lanžhot, and June and July 2020 in Järvselja (Fig. 2). TLS scans were acquired in a 30 m by 30 m plot using a Leica P40 ScanStation with a vertical field of view of 305 degrees (centered at the zenith). The laser beam had a wavelength of 1550 nm with a divergence of 0.23 mrad and a diameter of 6 mm at the instrument. Measurements were done at 16 positions along 4 by 4 grid points with 10 m spacing inside the stands at heights ranging between 1.4 and 1.8 m. Polystyrene spheres were placed in a 40 m by 40 m grid spaced 10 m apart over the stand (with additional spheres around the edges) for coregistration of the TLS scans. The data collection was done under calm wind conditions and dry weather.

From the TLS point clouds, we computed five forest structure variables: the LAI, the clumping index (CI), the canopy gap fraction (gf), the mean canopy height (h_mean) and the standard deviation of the canopy height (h_sd).

The 16 scans of each stand were co-registered in Leica Cyclone (v9.4.0) to sub-centimeter accuracy. The resulting point cloud was saved at full resolution and a downsampled resolution for semantic segmentation. Downsampling was done to 2 cm spacing. Individual trees were segmented using the method of Wang et al. (2021). Leaf and wood points were segmented using the unsupervised LeWoS method (Wang et al., 2020; Wang, 2024), which also produced a digital elevation model, excluded ground points and normalized the height coordinates of the point cloud. For further processing, a horizontal bounding box was used to crop the point cloud to a 25 m by 25 m area with the same center and orientation as the TLS grid (Fig. 3).

The mean height and its standard deviation of each stand were calculated from the normalized heights of each segmented tree within the bounding box. The LAI was calculated from a voxel-based measurement of leaf area density using the full resolution point cloud and a ray tracing approach following Pimont et al. (2018). To obtain the CI, a second ray tracing step was implemented to calculate angular canopy gap fractions over different orientations, and subsequently the

Table 1
Characteristics of forest plots in each study area. Tree height, diameter at breast height, basal area, stem number and dominant tree species were measured in the field, forest floor fractional cover was computed from nadir-view field photographs, leaf area index and first echo cover index were derived from terrestrial and airborne LiDAR scanning, respectively. The values correspond to mean and standard deviation (±SD) per study area.

		Study areas			
		Bílý Kříž	Lanžhot	Järvselja	Hyytiälä
Tree height (m)		32.77 ±9.04	30.67 ±8.62	24.67 ±8.00	20.98 ±5.75
Diameter at breast height (cm)		37.89 ±12.15	43.13 ±21.63	22.05 ±10.76	21.07 ±7.66
Basal area (m^2 ha^{-1})		50.23 ±19.41	32.55 ±14.21	25.21 ±13.65	22.89 ±8.60
Stem number (ha^{-1})		576.00 ±150.09	554.67 ±418.45	1175.11 ±694.44	1016.53 ±638.85
Leaf area index		2.03 ±0.32	3.19 ±0.36	2.26 ±0.56	1.96 ±0.83
First echo cover index		0.88 ±0.07	0.91 ±0.13	0.82 ±0.21	0.75 ±0.07
Number of plot per dominant tree species	*Picea abies* (L.) H. Karst (Norway spruce)	4		1	5
	Pinus sylverstris L. (Scots pine)			2	6
	Betula sp (birch; B. *pendula* Roth, B. *pubescens* Ehrh.)			2	4
	Quercus sp (oak; *Q. robur* L., *Q. petraea* (Matt.) Liebl.)		6		
	Alnus glutinosa (L.) Gaertn (European black alder)			2	
	Populus tremula L. (European aspen)		1	2	
	Carpinus betulus L. (European hornbeam)		1		
	Fraxinus sp (ash; *F. excelsior* L., *F. angustifolia* Vahl)		1		
Forest floor fractional cover	Vascular plant	0.21 ±0.29	0.23 ±0.20	0.60 ±0.25	0.54 ±0.16
	Non-vascular plant	0.06 ±0.07	0.00 ±0.01	0.07 ±0.11	0.13 ±0.12
	Intact plant litter	0.73 ±0.35	0.58 ±0.19	0.30 ±0.19	0.33 ±0.16
	Decomposed plant litter	0.00 ±0.00	0.18 ±0.17	0.03 ±0.08	0.00 ±0.00
	Lichen	0.001 ±0.001	0.000 ±0.000	0.001 ±0.001	0.004 ±0.005

Table 2
List of forest structure metrics derived from Terrestrial Laser Scanning (TLS), Airborne Laser Scanning (ALS) and Synthetic Aperture Radar (SAR) data, and their corresponding abbreviations used in the text hereafter.

Forest structure metric	Abbreviation	Data source
Leaf area index	LAI	TLS
Clumping index	CI	TLS
Canopy gap fraction	gf	TLS, ALS
Mean canopy height	h_mean	TLS, ALS
Standard deviation of the canopy height	h_sd	TLS, ALS
First echo cover index	FCI	ALS
VV backscatter coefficient	VV	SAR
Backscatter ratio VH/VV	VHVV	SAR
Coherence from the VV polarization	VV_coh	SAR
Coherence from the VH polarization	VH_coh	SAR

effective LAI. The ratio of the measured LAI to the effective LAI is the CI. The canopy gap fractions derived at angles from 0 to 81 degrees were highly correlated, therefore, we selected the gap fraction at 81 degrees. Readers are referred to Schraik et al. (2023) for further details on the TLS data collection, pre-processing, and calculation of LAI and CI.

2.3.2. Airborne laser scanning

The ALS acquisitions were conducted in July 2019 in Hyytiälä and Järvselja, and in September 2019 in Lanžhot and Bílý Kříž (Fig. 2). We used a Riegl LMS Q780 waveform-recording sensor (Riegl Gmbh, Austria) mounted on a Cessna C208B aircraft. The laser wavelength was 1064 nm, and the beam divergence was 0.25 mrad. Flight altitude was approximately 1 km, maximum zenith angle of the lidar pulses was ≈30 degrees, and the overlap of the flight lines varied between 75 and 87%. Data acquired at zenith angles larger than 20 degrees were removed, because oblique angles can affect the pulse penetration to the canopy. The pulse densities of data used in our analyses were 7, 7, 20, and 20 pulses/m^2 in Lanžhot, Bílý Kříž, Järvselja, and Hyytiälä, respectively. The raw waveform data were processed using Riegl's software suite (RiProcess v1.8.4, RiAnalyze v6.2.2, RiWorld v5.1.3, and

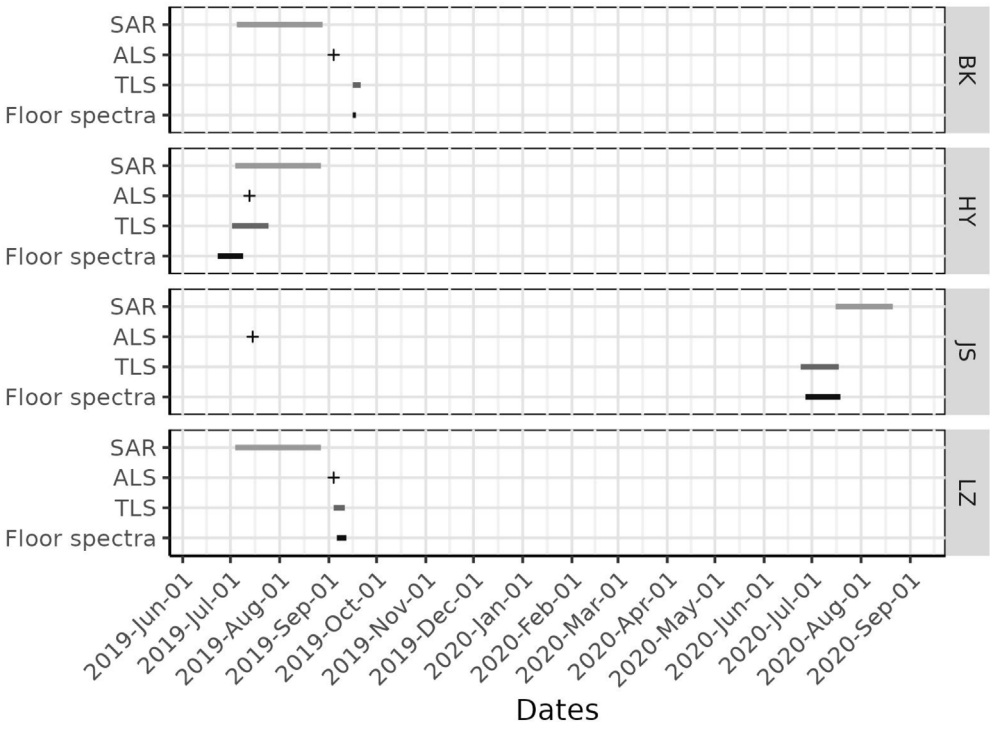

Fig. 2. Acquisition periods per data type and study area. HY = Hyytiälä, JS = Järvselja, BK = Bílý Kříž, LZ = Lanžhot. In Hyytiälä, the forest floor spectra of three out of fifteen plots were measured at the end of June 2018. They were measured under phenological conditions similar to those of the 2019 field campaign.

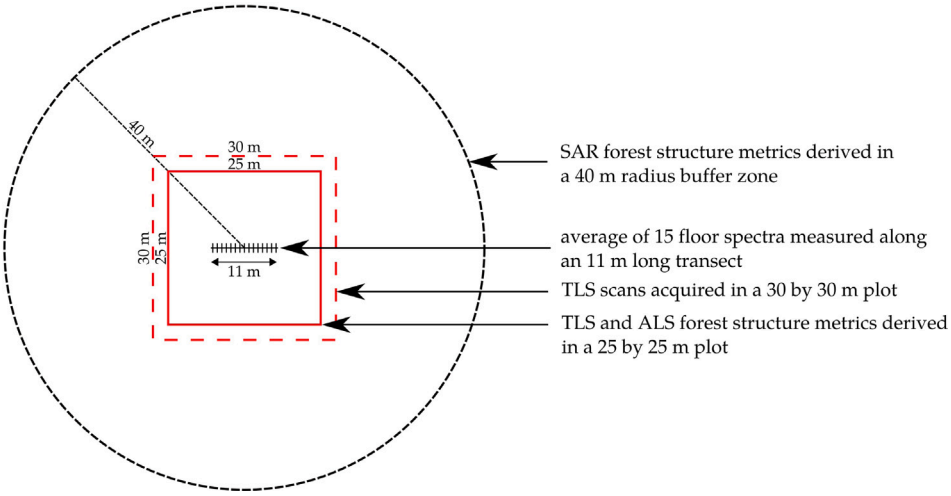

Fig. 3. Spatial configuration of the data sampling in our study plots.

GeoSysManager v2.0.8), resulting in point clouds georeferenced into the ETRS89 coordinate system with UTM projection (ESPG 25833 for Lanžhot and Bílý Kříž, and EPSG 25835 for Hyytiälä and Järvselja) and ellipsoid heights. A raster digital elevation model (DEM) representing the ground surface was produced at 1 m resolution, using echoes that had been classified as ground with LASTools software. Data collection and processing steps have been detailed in Hovi et al. (2023).

From the ALS point clouds, we computed four forest structure variables: First echo cover index (FCI), mean canopy height (h_mean), standard deviation of canopy height (h_sd), and canopy gap fraction (gf). The FCI, h_mean, and h_sd metrics were calculated using the standard area-based approach (Næsset, 2002), in which echoes are extracted from a predefined area, their height from ground is calculated, and metrics are then calculated from the height-normalized point cloud. We used a height threshold of 1.5 m to separate canopy and ground echoes. The h_mean and h_sd were calculated using all LiDAR echoes obtained from the canopy. The FCI was calculated as the number of first echoes obtained from the canopy divided by the total number of first echoes. We used a plot size of 25 m by 25 m (Fig. 3), because it provided the best predictive models among the range of plot sizes tested from 10 to 100 m (Appendix C). The canopy gap fraction was calculated from synthetic hemispherical photographs generated from the LiDAR data by assuming that each LiDAR echo represents an opaque sphere (Varhola et al., 2012; Hancock et al., 2014; Webster et al., 2020). There were 16 photographs per stand, and they were placed in a similar 4 by 4 grid as used for the TLS data. We derived the canopy gap fraction at zenith angles between 75 and 90 degrees to be consistent with the TLS-derived gf metric calculated at 81 degrees. The calculation of synthetic hemispherical photographs has been described in detail in Hovi et al. (2023).

2.3.3. Sentinel-1 images

Sentinel-1 (S1) image time series in C-band (5.405 GHz) were downloaded (SentiWiki, 2024) at the peak growing season (July and August), from the same year as the forest floor spectra and TLS acquisitions (Fig. 2). The goal was to characterize the forest structure among the four study areas in a homogeneous way, while the forest canopy is at the same phenological stage so the metrics are comparable. S1 images were excluded from the time series when daily precipitation exceeded 1 mm (Appendix B) since SAR backscatter signal is affected by leaf and branch moisture (Westman and Paris, 1987). S1 images were downloaded in Interferometric WideSwath (IW) in the WGS 84 coordinate system (EPSG 4326). All images were acquired on ascending mode, meaning a revisit time of 6 days for our study areas.

From the SAR time series, we computed four forest structure variables: VV backscatter coefficient (VV), backscatter ratio VH/VV (VHVV), coherence from the VV polarization (VV_coh) and coherence from VH polarization (VH_coh). Level-1 Ground Range Detected (GRD) providing amplitude of the signal was used to derive the VV and VH backscatter coefficients, while Level-1 Single Look Complex (SLC) containing both amplitude and phase information was needed to compute coherence images.

As VV and VH polarizations were strongly correlated across the 37 stands analyzed, we selected only the VV backscatter coefficient. Previous studies have compared the potential of VV and VH polarizations from C-band to map forest canopy characteristics in boreal (Ge et al., 2023) and temperate forests (Hoffmann et al., 2022; Borlaf-Mena et al., 2023) and concluded that there are very slight differences in the accuracy of results.

The GRD images were acquired from the Google Earth Engine (GEE) "COPERNICUS/S1_GRD" collection. The resolution was 20 × 22 m (rg×az) and the pixel spacing was 10 × 10 m (rg×az). We used 6, 8, 5 and 9 S1 GRD images for Bílý Kříž, Lanžhot, Järvselja and Hyytiälä, respectively at relative orbit numbers 175, 73, 160 and 160 (Fig. 2 and Appendix B). The GEE collection provides S1 images already preprocessed with thermal noise removal, radiometric calibration and terrain correction steps. We converted the provided VV and VH backscatter coefficients from sigma nought to gamma nought values since gamma nought reduce the influence of topography on the backscatter and improve forest mapping in undulated terrain (Atwood et al., 2012; Dostalova et al., 2022).

The SLC images were downloaded from the Copernicus Data Space Ecosystem (Copernicus Data Space Ecosystem, 2023). The resolution was from 2.7 × 22 m to 3.5 × 22 m (rg×az) and the pixel spacing was 2.3 × 14.1 m (rg×az). We downloaded two SLC images per site using the early July date as a slave image (Appendix B). Coherence images were calculated using the SNAP software from the following processing steps: (1) TOPSAR-Split, (2) Applying-Orbit-File (Sentinel Precise Auto Download, polynomial degree of 3), (3) Back Geocoding (Copernicus 30 m Global as DEM, bilinear interpolation as resampling method), (4) Coherence estimation (Copernicus 30 m Global as DEM, orbit interpolation degree of 3, 10 pixels and 3 lines used for coherence estimation, the degree of "Flat Earth" polynomial was 5, the number of "Flat Earth" estimation points was 501), (5) TOPSAR-Deburst, and (6) Terrain Correction (Copernicus 30 m Global as DEM, bilinear interpolation as resampling method).

We averaged the pixel values of the SAR forest structure metrics in a buffer zone of 40 m radius around the central coordinates of the study stands (Fig. 3). Sentinel-1 was the only sensor in this study allowing for the derivation of aggregated metrics for the same period, while forest floor spectra, ALS, and TLS were acquired on a single date at different times due to field work constraints. The 40 m radius was used because it provides the best predictive models among the range of radii tested from 10 to 100 m (Appendix C). As the stands were located in homogeneous forest patches and at least 43 m apart, the 40 m radius windows represent a similar forest type per stand while avoiding overlaps between them.

Table 3
For the exploratory analysis, we concentrated on the 12 listed Sentinel-2 (S2) spectral bands (Sentinel-2 MSI Technical Guide, 2024).

Sentinel-2 band name	Wavelength (nm)
Coastal aerosol	443
Blue	493
Green	560
Red	665
Vegetation red-edge 1 (RE1)	704
Vegetation red-edge 2 (RE2)	740
Vegetation red-edge 3 (RE3)	783
Near-infrared (NIR)	833
Narrow Near-infrared (NIR)	865
Near-infrared (NIR) - water vapor	945
Shortwave infrared 1 (SWIR1)	1614
Shortwave infrared 1 (SWIR2)	2202

3. Methods

3.1. Exploratory part

The purpose of the exploratory part was to analyze relationships between forest structure metrics and forest floor spectral properties focusing on 12 Sentinel-2 (S2) spectral bands (Table 3). The "SWIR - Cirrus" band of S2 was omitted due to high noise in the forest floor spectral measurements around 1375 nm caused by absorption of electromagnetic radiation by water in the atmosphere.

The methodological workflow was designed following recommendations by Tredennick et al. (2021) and is illustrated in Fig. 4a. Linear mixed-effect models for identifying relationships between forest structure metrics and reflectance factors of forest floor at each spectral band were computed using the lme function from the lme4 R package (Bates et al., 2015). The study area was used as a random effect on the intercept and slope to take into account the clustered structure of the dataset. We proceeded in two steps to avoid highlighting spurious relationships by reducing the number of input variables in the models. First, we computed Pearson correlation coefficients between the forest floor reflectance factors in different spectral bands and forest structure variables. Forest structure variables with a p-value less than 0.1 were considered as potentially important and selected as input in the linear mixed-effect model. Next, we assessed the importance of each forest structure variable individually through variable selection in the mixed-effect model. We used the drop1 function from the R stats package (R Core Team, 2023) that consists of eliminating a single variable from the model and comparing the performance of the full model with the series of reduced models. We used the chi-squared test to assess the significance of the difference between the models. A p-value from the chi-squared test below 0.05 indicated significant relationships between forest structure and reflectance factors at certain wavelengths.

3.2. Predictive part

We predicted the forest floor reflectance factors across the full spectrum using three different sets of predictor variables: (1) TLS, ALS and SAR metrics alone, (2) combined ALS and SAR, and (3) combined ALS, TLS and SAR data. We used linear mixed-effect models for the prediction, and tested the accuracy of the models with an independent data set (Fig. 4b).

We computed a linear mixed-effect model for each wavelength and for each sensor configuration specified in cases (1)–(3) using the R glmmLasso package (Groll, 2023). In order to be comparable with each other, the reflectance factors at each spectral band and predictive forest structure metrics were mean normalized (i.e. centered by subtracting the mean and scaled by dividing by the standard deviation). First, the 37 stands were randomly split into training and test datasets with a 70/30 ratio. Then, a 5-fold cross-validation was done on the training dataset to perform the model selection, i.e., lasso regularization and

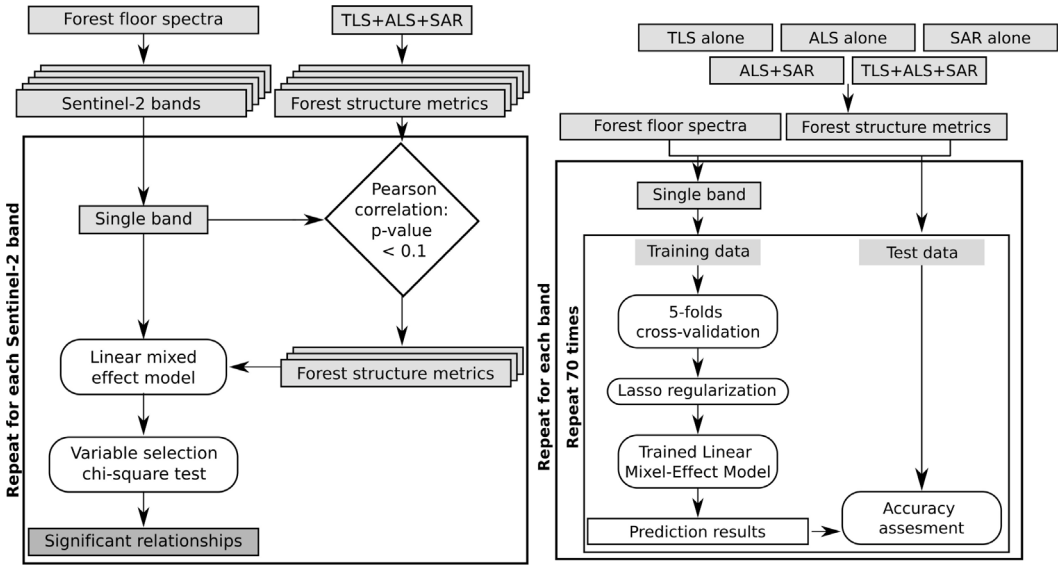

(a) Exploratory part workflow (b) Predictive part workflow

Fig. 4. (a) Exploratory part workflow: Linear mixed-effect models identified relationships between forest structure metrics and forest floor reflectance factors. Pearson correlation coefficients were computed, and variables with a p-value < 0.1 were included in the models. The significance of the relationships was assessed using the chi-squared test (b) Predictive part workflow: Linear mixed-effect models were employed to predict forest floor reflectance factors from forest structure metrics derived from (1) TLS alone, (2) ALS alone (3) SAR alone (4) combined ALS and SAR data, and (5) combined TLS, ALS and SAR data. The 37 stands were split into training and test datasets, then 5-fold cross-validation was used to select the predictors through lasso regularization and estimate the parameters of the linear mixed-effect model. Finally, we evaluated the model accuracy with the test dataset. This process was repeated 70 times to address the small sample size.

regularization parameter optimization. Lasso regularization was used to perform automated variable selection as it can remove variables from the model by shrinking their coefficients to zero (Tibshirani, 1996). The regularization parameter, lambda, was tested on a sequence from 0 to 100 with a constant step length of 5, and set to minimize the mean squared error over the K cross-validation folds. Then, the linear mixed-effect model was refitted using the entire training dataset with the optimal lambda value. To measure the model accuracy, we computed the Root-Mean Squared Error (RMSE), bias, relative absolute error (RAE) and coefficient of determination (R^2) using the independent test dataset using the following equations:

$$\mathrm{RMSE}(y,\hat{y}) = \sqrt{\frac{\sum_{i=0}^{N-1}(y_i-\hat{y}_i)^2}{N}} \tag{1}$$

$$\mathrm{RAE}(y,\hat{y}) = \frac{\left[\sum_{i=1}^{n}(\hat{y}_i-y_i)^2\right]^{1/2}}{\left[\sum_{i=1}^{n}(y_i)^2\right]^{1/2}} \tag{2}$$

$$R^2(y,\hat{y}) = 1 - \frac{\sum_{i=1}^{N}(y_i-\hat{y}_i)^2}{\sum_{i=1}^{N}(y_i-\bar{y})^2} \tag{3}$$

where $\hat{y}$ corresponds to the mean of the observed values and y_i to the predicted value for the ith observation in the dataset.

$$\mathrm{Bias}\left(\hat{\theta}_n\right) = E\left(\hat{\theta}_n\right) - \theta \tag{4}$$

where $\hat{\theta}$ corresponds to the estimator of θ.

The RMSE represents the average magnitude of the square of the errors between predicted and test values. The RAE is a ratio ranging from 0 to 1 and comparing a mean error (residual) to errors produced by a naive model. An RAE lower than 1 means the model predict better results than a trivial model. The R^2 measures the proportion of the variance in the dependent variable (forest floor reflectance factors) that can be explained by the independent variables (forest structure metrics). The bias indicates whether the prediction model consistently underestimates or overestimates the test values, represented by negative and positive values, respectively.

Due to the small sample size, we repeated the above process 70 times, i.e., we randomly split the data into 70 pairs of training and test datasets and performed the analysis from the model selection to the model evaluation in each of them (Fig. 4b). To allow sensor performance comparisons, the same 70 splits were used for each sensor configuration. For each wavelength, we averaged the resulting RMSE, bias, RAE and R^2. A mean normalization was applied to the reflectance factors. Consequently, an RMSE of 1 would mean that it is equal to the standard deviation of the reflectance factors.

The 37 sampled stands against the 13 input covariates may lead to over-fitting, as regularization and internal cross-validation do not prevent over-fitting when the number of covariates exceeds the number of independent observations (Tredennick et al., 2021). Therefore, we reduced the number of input variables in the combined ALS, TLS and SAR model including only the forest structure metrics identified as the most important ones from the predictive models using TLS alone, ALS alone and SAR alone.

4. Results

4.1. Exploratory part

We identified a total of nine forest structure metrics that were potentially associated with forest floor reflectance factors (the nine columns of Table 4). Three TLS-derived forest structure metrics (LAI, CI and h_sd) and three SAR-derived metrics (VV, VHVV, VV_coh) were potentially associated with forest floor reflectance factors in the visible, RE, NIR or SWIR spectral region. Three ALS-derived metrics (FCI, h_mean, h_sd), were potentially correlated with forest floor reflectance factors in the red-edge, NIR and SWIR regions. Among all these potentially associated metrics, TLS-derived CI and LAI, and SAR-derived VV and VHVV were significantly connected to reflectance factors at four and seven S2 spectral bands, respectively. None of the ALS metrics was significant. In four spectral bands of S2 (443 nm, 493 nm, 560 nm, 945 nm), forest floor reflectance factors were not significantly correlated with any forest structure metrics.

Table 4
Estimated coefficients from the linear mixed-effect models per Sentinel-2 spectral band by eliminating a single variable from the full model at a time. The nine forest structure metrics (columns) had a Pearson correlation with a p-value below 0.1 and were selected for the linear mixed effect model. Parameters in bold highlight the significant relationships demonstrated between forest structure metrics and S2 spectral bands. A forest structure metric with a significant p-value (<0.05) means that removing it from the full model significantly reduced the performance of the model.

	TLS			ALS			SAR		
Input metrics\ HCRF (nm) and associated S2 bands	LAI	CI	h_sd	FCI	h_mean	h_sd	VV	VHVV	VV_coh
443 (aerosols)		0.013					0.003	−0.001	
493 (blue)		0.017					0.004		
560 (green)	−0.001								
665 (red)		0.061					**0.014***	0.000	
704 (RE1)		**0.069***							
741 (RE2)	**0.06***	0.088	0.036	−0.179	−0.007	−0.016	**−0.062****		0.288
783 (RE3)	**0.065***	0.091	0.038	−0.197	−0.008	−0.018	**−0.071****		0.343
833 (NIR)	**0.063***	0.116	0.037	−0.199	−0.007	−0.018	**−0.069****		0.346
865 (NIR)	0.053		0.033	−0.13	−0.006	−0.019	**−0.063****		0.349
945 (vapor)	−0.006				−0.001	−0.007			0.084
1614 (SWIR1)		0.195		−0.006			0.011	**−0.029***	
2202 (SWIR2)	−0.022	0.128		0.026	−0.001	0.008	0.021	**−0.025***	

* Corresponds to p-values from 0.01 to 0.05.
** Corresponds to p-values less than 0.01.

In order to visualize the relationships between forest structure metrics and reflectance factors at S2 spectral bands, we plotted linear regressions of the significant relationships by study area (Fig. 5). Relationships between forest structure and forest floor reflectance factors showed differing trends between sites (Fig. 5). Overall, the relationships between SAR-derived metrics and the reflectance factors at S2 spectral bands appeared stronger for coniferous stands compared to broadleaves.

4.2. Predictive part

When predicting the forest floor reflectance factors across the full spectrum, the active remote sensors achieved the best predictions at wavelengths from 700 to 1000 nm, and from 1504 to 2500 nm (i.e., RE, NIR and SWIR regions) (Fig. 6). Conversely, the weakest predictions were observed in the visible (350–700 nm) and SWIR (1200 and 1336 nm) regions. The combination of ALS, TLS and SAR metrics predicted the forest floor spectra better than any sensor alone or ALS and SAR combined (Fig. 6). The performance of ALS, TLS and SAR metrics was dependent on the spectral region. When used alone, SAR metrics led to highest model accuracy for reflectance factors at RE and NIR bands, and TLS or SAR metrics for SWIR (Fig. 6). ALS was the least accurate in predicting reflectance factors at SWIR bands, and TLS was the least accurate for reflectance factors at NIR bands (Fig. 6). The predictive part confirmed the potential of CI, VV and VHVV to predict forest floor spectral properties (Fig. 7, Appendices D, E). TLS-derived CI and SAR-derived VHVV were the strongest contributors to the predictive models in the SWIR regions (Fig. 7d). SAR-derived VV was the strongest metric to predict reflectance factors at NIR bands (Fig. 7d). Height-related forest structure metrics (h_mean, h_sd) from ALS and TLS, and coherence (VV_coh, VH_coh) from SAR were weak contributors (Fig. 7a and b).

5. Discussion

5.1. Links between forest floor characteristics and forest structure metrics derived from active remote sensing data

While previous studies have demonstrated the potential of passive optical remote sensing data for mapping forest floor spectral properties (Markiet and Mõttus, 2020; Hovi et al., 2023), this work reveals the interesting potential of TLS, ALS and SAR data. It links remote sensing studies aimed at describing forest structure using TLS, ALS and SAR (Schraik et al., 2023; Acebes et al., 2021; Di Stefano et al., 2021; Guo et al., 2020; Holzwarth et al., 2020; Bruggisser et al., 2021; Rosenqvist et al., 2021) and ecological studies reporting the relationships between overstory structure and understory vegetation in forests (Messier et al., 1999; Barbier et al., 2008; Majasalmi and Rautiainen, 2020; De Pauw et al., 2022). This study demonstrated for the first time relationships between forest structure metrics derived from active remote sensing technologies and forest floor spectral properties. The use of active remote sensing data offers solutions to some limitations of passive optical data, such as uncertainty in retrieving forest floor spectral properties in dense forests (Hovi et al., 2023) and strong dependence on illumination conditions.

The relationships that we identified between forest structure and forest floor spectral properties can be explained based on previous studies demonstrating links between understory vegetation composition, forest floor reflectance factors and light availability at the forest floor. High NIR and low visible and SWIR reflectance factors of forest floor correspond to high proportion of vascular plants and low proportion of non-vascular plants and intact litter (Forsström et al., 2023), and NIR reflectance factors have been shown to increase with the fertility of the forest floor (i.e., higher proportion of vascular plants) (Markiet and Mõttus, 2020). Furthermore, Hallik et al. (2009) have demonstrated that the herb–moss layer in forests tends to be brighter in the visible wavelength region when the canopy above is more closed. Finally, the cover of vascular plants has been demonstrated to grow with increasing light availability, which in turn leads to low reflectance factors of the forest floor at visible and SWIR bands and high reflectance factors in NIR bands (Forsström et al., 2023). The same study reported that the amount of intact litter decreases with increasing light availability, and leads to high reflectance factors in visible and SWIR bands and low reflectance factors in NIR.

Our results unveiled that TLS and SAR forest structure metrics are promising for predicting forest floor spectra in NIR and SWIR regions. Overall, the active remote sensors achieved the best predictions in RE, NIR and SWIR regions. The higher potential of ALS, TLS and SAR for certain spectral regions supports previous studies estimating forest floor characteristics from hyperspectral data (Rautiainen et al., 2011; Markiet and Mõttus, 2020) and hemispherical photographs (Forsström et al., 2023). Forsström et al. (2023), analyzing the relationships between the forest floor spectra and the light availability for the same four study areas as in our study, reported weak relationships in the visible, and strongest relationships in the SWIR from 2094 to 2316 nm.

Our results confirm that new types of tree canopy characteristics derived from TLS, ALS and SAR data also highlight clear connections between forest overstory structure and understory composition

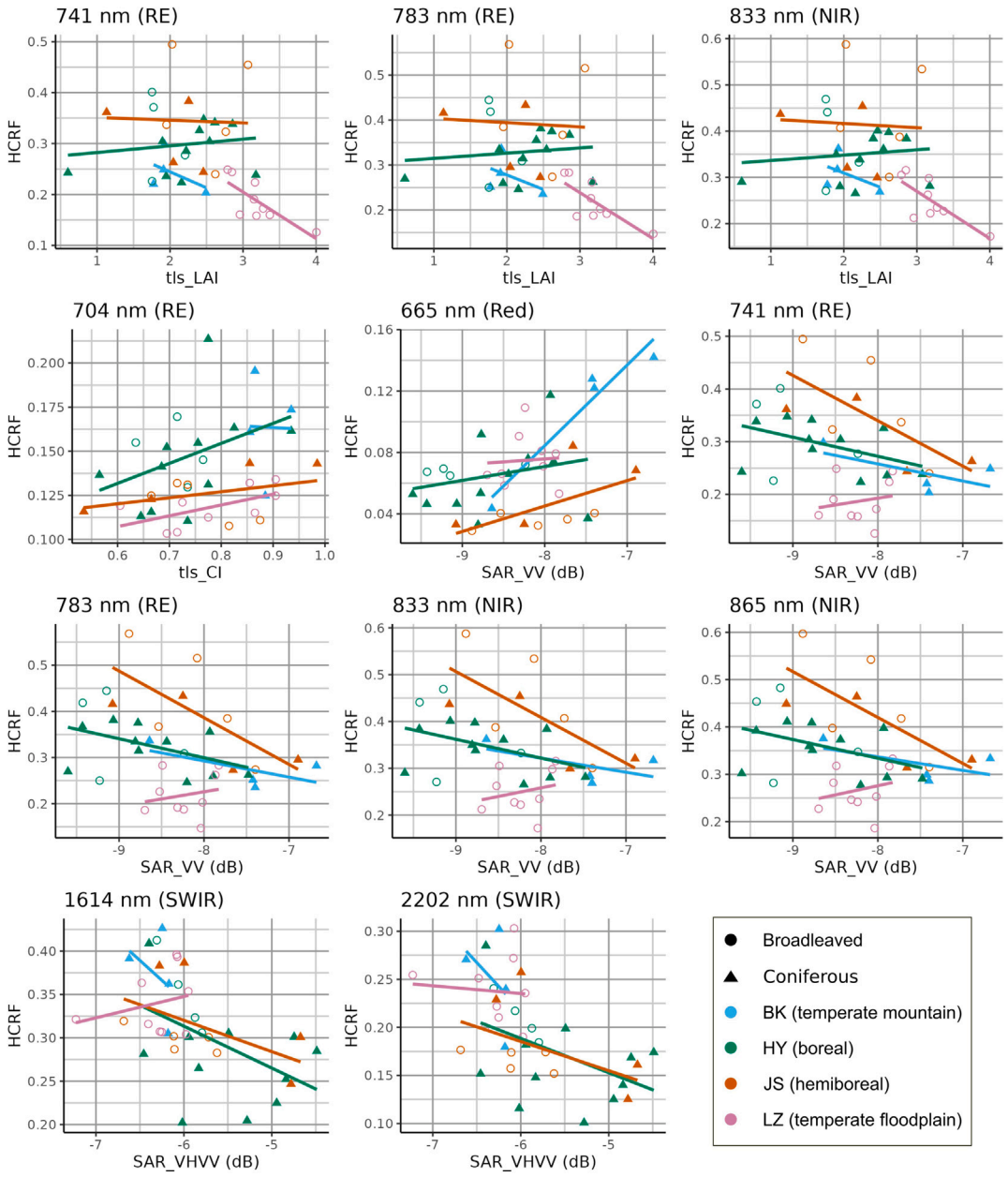

Fig. 5. Relationships between forest structure metrics leaf area index (LAI) and clumping index (CI) (from TLS) and VV backscatter coefficient and VH/VV ratio (from SAR) with hemispherical-conical reflectance factors (HCRF) of the forest floor (interval between 0 and 1) at different Sentinel-2 (S2) spectral bands, based on the final linear mixed-effect models (Table 4). We show only those relationships demonstrated as significant by the exploratory part: three spectral bands of S2 for leaf area index (LAI), one for clumping index (CI) and five for the VV backscatter coefficient (VV) and two for the VH/VV ratio (VHVV). Linear regressions are represented by study areas, with Bílý Kříž, Hyytiälä, Järvselja and Lanžhot labeled BK, HY, JS and LZ. The forests dominated by broadleaved and coniferous trees are represented with circles and triangles, respectively.

in temperate and boreal forests, complementing the traditional forest inventory variables (Messier et al., 1999; Barbier et al., 2008; Majasalmi and Rautiainen, 2020). The exploratory part highlighted nine potentially important forest structure metrics for predicting the spectral properties of forest floor and identified TLS-derived CI and LAI, and SAR-derived VV and VHVV as significantly connected to forest floor reflectance factors at certain S2 bands. The predictive part confirmed the potential of CI, VV and VHVV (Fig. 7, Appendices D, E). Also the predictory part revealed FCI and gf from ALS as important predictors of forest floor reflectance factors.

TLS-derived CI was positively correlated to reflectance factors at visible and SWIR bands. CI values of 1 represent randomly distributed canopies, while lower CI values indicate clumped canopies (Fang, 2021). Clumped stands allow more light to reach the forest floor compared to a random leaves distribution (Schraik et al., 2023). Therefore, low CI values indicate clumped stands leading to more light reaching the forest floor. This allows a higher proportion of vascular plants which, in turn, induces low visible and SWIR reflectances factors. Similarly, SAR-derived VV was positively correlated to forest floor reflectance factors at visible and SWIR regions and negatively correlated to reflectance factors at RE and NIR. The C-band S1 SAR instrument operates at a center frequency of 5.405 GHz, therefore the signal interacts with small forest elements of size around 5 cm corresponding mainly to leaves and twigs (Le Toan et al., 1992). The contribution of shrub understory to the C-band signal appeared negligible in forest, even in open canopy (Westman and Paris, 1987): VV from C-band has been shown to be positively correlated to tree leaf and stem surface areas in a temperate coniferous forests. Moreover, VV backscattering increases with increasing LAI in boreal forests (Manninen, 2012) and the mean power of backscattering coefficient at C-band increases with the density

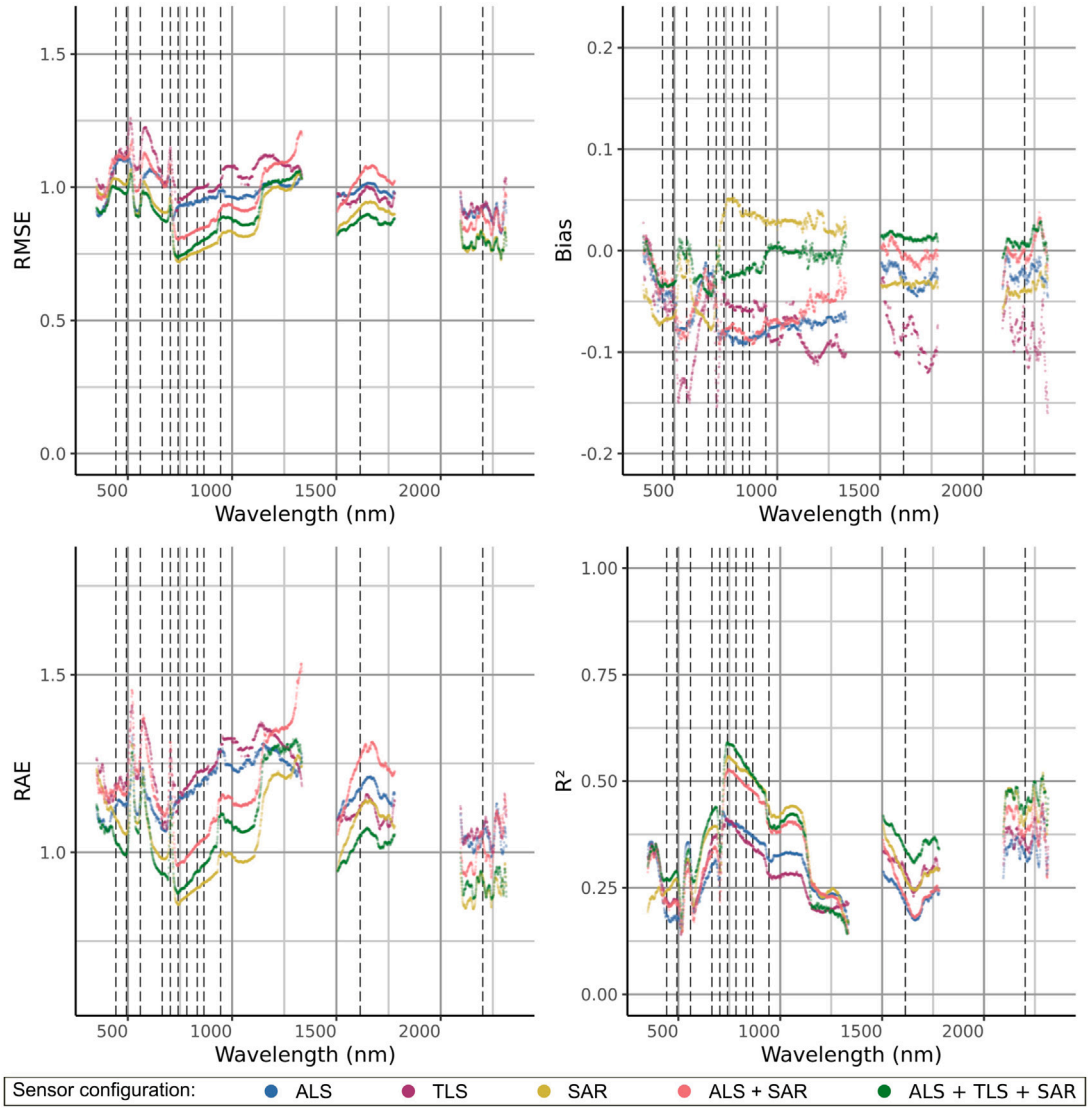

Fig. 6. Average Root-Mean Square Error (RMSE), bias, Relative Absolute Error (RAE) and coefficient of determination (R^2) values for the five sensor configurations calculated from the 70 pairs of training and test sets. Response variables were normalized per wavelength before analyses to be comparable. Normalized forest floor reflectance factors were zero-centered with a standard deviation of 1. Vertical dashed lines indicate the wavelengths corresponding to the centers of the Sentinel-2 bands (443, 493, 560, 665, 704, 740, 783, 833, 865, 945, 1614, 2202 nm, corresponding to "coastal aerosol", "blue", "green", "red", "vegetation red-edge 1" (RE1), RE2, RE3, "near-infrared" (NIR), "narrow NIR", "NIR-water vapor", shortwave infrared 1" (SWIR1) and SWIR2 bands. (For interpretation of the references to color in this figure legend, the reader is referred to the web version of this article.)

of leaves in coniferous forests (Li et al., 2019). Therefore, we assume that low VV indicates less dense and more open canopy cover, leading to higher light availability at the forest floor favorable for vascular plants but not intact litter, and hence corresponding to low visible and SWIR and high NIR reflectance factors from the forest floor. The stronger relationship between forest floor spectra and VV in coniferous-dominated than in broadleaved-dominated stands (Fig. 5) could be due to higher VV in coniferous than in deciduous forests (Dostálová et al., 2016) or weak relationships between light availability and forest floor spectral properties in stands dominated by broadleaf trees compared to coniferous trees (Forsström et al., 2023). In conclusion, low CI and VV values suggest forest floor vegetation composed mainly of vascular plants and a small proportion of intact plant litter.

The potential of ALS-derived forest structure metrics to predict forest floor reflectance factors was lower than those from TLS or SAR, and no significant relationships were revealed in the exploratory part (Table 4). In Bílý Kříž and Järvselja, disparities in the temporal acquisition periods of the sensors could have an impact on the relationships between the forest floor spectral properties and the different sensors. In our study, the ALS acquisitions were conducted with a temporal offset to the collection of forest floor spectra, while the TLS were conducted at the same location at the same time, and the SAR S1 images were downloaded and averaged throughout the corresponding growing season (Fig. 2). We assume that CI derived from TLS was the most contributing metric among the TLS- and ALS-derived forest structure metrics (i.e., height, canopy gap fraction, FCI, LAI) because it was the only metric to take full advantage of the 3D structure of the point cloud by quantifying the spatial distribution of canopy elements. Finally, the weak relationships between height-related metrics derived from ALS and TLS and forest floor spectra (Table 4, Fig. 7a and b) could be due to their disconnection from light availability, which is a key parameter that determines forest floor reflectance factors.

5.2. Future considerations

This study is based on a unique dataset, including 37 stands in four distinct study areas covering the vegetation gradient from temperate

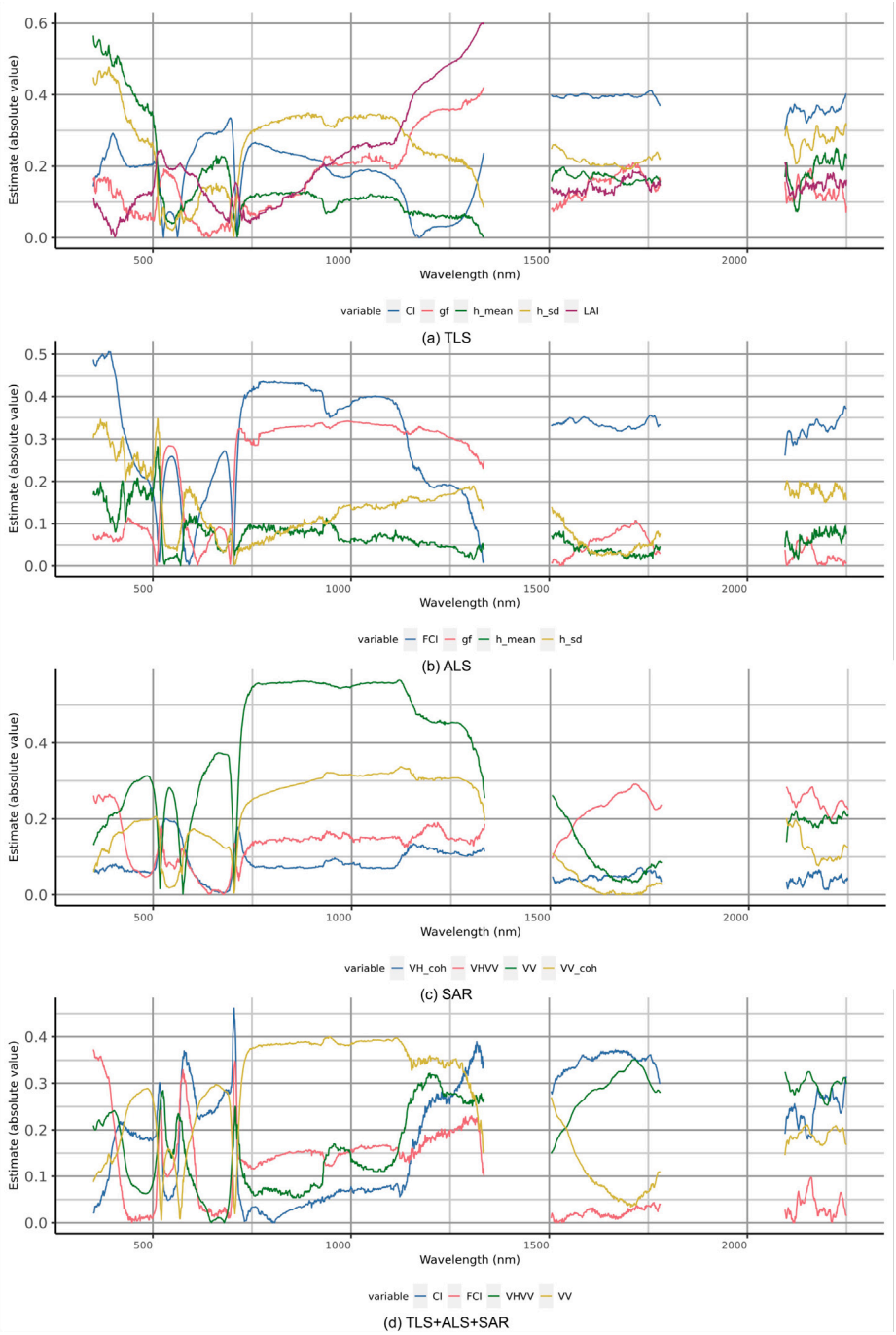

Fig. 7. Absolute average coefficients of forest structure metrics calculated from the 70 pairs of training and test sets when using (a) TLS alone, (b) ALS alone, (c) SAR alone and (d) combination of TLS, ALS and SAR. Coefficients were optimized using lasso regularization.

to boreal forest with field measurements. Extensive forest inventories typically do not measure the spectral properties of forest floor, and while they might include some forest floor characteristics, these measurements rarely coincide with ALS or TLS data. Such a detailed and globally unique dataset represents a significant advance in the comparison of ALS, TLS and SAR sensors and has allowed investigating the potential of active sensors and forest structure metrics derived from their data to predict forest floor spectral properties. Future efforts should aim to obtain larger samples of plots along a forest structure gradient in order to better understand the complex links between forest structure and forest floor spectral properties.

Metrics associated with forest height (h_mean, h_sd) show limited potential, meaning that vertical structure of temperate and boreal forests plays a lesser role in forest floor characteristics. The development of structural metrics to comprehend variations in forest floor spectral properties should focus on horizontal forest structure. Additionally, considering interactions between forest structure metrics could explain the responses of different plant functional types, e.g. conifers and broadleaves, vascular and non-vascular plants or dominating tree species (Tredennick et al., 2021).

In the future, the retrieval of forest floor reflectance spectra could benefit from a synergy of passive and active remote sensing technologies. Previous studies have already exploited the complementarity of airborne LiDAR and passive optical data to identify vegetation communities in coniferous forests (Su et al., 2016), to discriminate shrubs from trees (Zahidi et al., 2015) and to predict forest floor

reflectance factors (Hovi et al., 2023). Our study showed that forest structure metrics derived from SAR data should also be explored as this would open up more opportunities for upscaling the monitoring activities of forest floor vegetation over large areas. The insensitivity of SAR data to cloud cover offers an advantage compared to optical images, particularly in boreal forests and mountainous areas where cloud cover is frequent (Xu et al., 2022). To extend our study to large spatial scale mapping of forest floor characteristics, the Sentinel-1 sensor would be valuable due to its large coverage, free availability and frequent revisits. Technically, mapping forest floor reflectance factors at the landscape scale can use a sliding circular window. Finally, future studies should explore L-band, which is more penetrative than the C-band, and quad-polarimetric sensors to understand the relationships between backscatter mechanisms and forest floor spectral properties.

In line with our motivation to focus on spectral properties because of their versatility in indicating many aspects of forest floor, a future consideration would be to predict directly forest floors' species composition (Kuusinen et al., 2023; Forsström et al., 2019; Rautiainen et al., 2011), surface fuel loads (Labenski et al., 2023; Stefanidou et al., 2020; Alonso-Rego et al., 2020), or moisture of mosses (Salko et al., 2023) using passive (spectral) or active remote sensing data. Dead wood has distinct spectral properties (Mercier et al., 2023; Juola and Rautiainen, 2022), and this information could be used to assess surface fuel loads.

Finally, the spectral properties of forest floor vegetation change during the growing season. For example, in hemiboreal and boreal forest, the most fertile forest type (herb-rich) shows the largest temporal dynamics in reflectance from early June to late September (Rautiainen et al., 2011; Nikopensius et al., 2015). Similar studies are lacking for the temperate forests of the Czech Republic. Monitoring changes in the understory using active remote sensing is feasible with synchronized forest structure and understory vegetation. De Pauw et al. (2022) suggested a short-term lag in the understory response to forest structure and a long-term lag in response to climate warming across Europe. Therefore, further studies are needed to understand these temporal dynamics. In conclusion, it is crucial to determine when the link between forest structure and forest floor spectral properties is the strongest and for how long the model accuracy remains acceptable.

6. Conclusion

Our results demonstrated that active remote sensing technologies are promising for predicting red-edge, near-infrared and shortwave infrared reflectance factors of the forest floor in temperate, hemiboreal and boreal forests. The best predictive model over the full spectrum was obtained by combining TLS, ALS and SAR data. SAR alone had the highest potential for reflectance factors at red-edge and near-infrared bands, achieving performances similar to those of the full sensor configuration. TLS alone was the most suitable sensor for predicting reflectance factors at shortwave infrared bands from 1504 to 1781 nm, while SAR and TLS both produced the best results for reflectance factors at shortwave infrared bands from 2094 to 2316 nm. Overall, the results highlight the potential of the clumping index derived from TLS, the VV polarization and the VH/VV ratio from Sentinel-1 to predict forest floor spectral properties. In the future, the accuracy of forest floor reflectance spectra predictions in temperate and boreal forests could benefit from a synergy of passive and active technologies. The promising results from TLS allow better understanding of the complex links between forest structure and forest floor characteristics, while the potential of Sentinel-1 data encourages to explore SAR satellite imagery for monitoring forest floor characteristics at large spatial scales. Large-scale estimates of forest floor characteristics will also help improve land surface models and climate predictions.

CRediT authorship contribution statement

Audrey Mercier: Writing – original draft, Visualization, Software, Methodology, Formal analysis, Conceptualization. **Mari Myllymäki:** Writing – review & editing, Methodology, Funding acquisition, Conceptualization. **Aarne Hovi:** Writing – review & editing, Investigation, Data curation. **Daniel Schraik:** Writing – review & editing, Investigation, Data curation. **Miina Rautiainen:** Writing – review & editing, Supervision, Project administration, Methodology, Funding acquisition, Conceptualization.

Declaration of competing interest

The authors declare that they have no known competing financial interests or personal relationships that could have appeared to influence the work reported in this paper.

Acknowledgments

We thank Petri Forsström, Bijay Karki, Jussi Juola and Ville Ranta for field work and field data processing, and Jan Hanuš, Karel Holouš, Tomáš Fabiánek, and Lukáš Fajmon for acquisition and processing of airborne data. Lucie Homolová kindly provided weather station data for the Czech Republic – the collection of the data was based on the use of Large Research Infrastructure CzeCOS supported by the Ministry of Education, Youth and Sports of CR within the CzeCOS program, grant number LM2023048. This study was mainly funded by the European Union – NextGenerationEU as part of the Research Council of Finland project ARTISDIG (decision numbers 348152 and 348154). MM's contribution was done under the Research Council of Finland's flagship ecosystem for Forest-Human–Machine Interplay—Building Resilience, Redefining Value Networks and Enabling Meaningful Experiences (UNITE) (Grant number 357909). This study has also received funding from the European Research Council (ERC) under the European Union's Horizon 2020 research and innovation programme (grant agreement No 771049). The text reflects only the authors' view and the Agency is not responsible for any use that may be made of the information it contains.

Appendix A. Forest floor spectra

See Fig. A.8.

Appendix B. Sentinel-1 dates and precipitation

See Fig. B.9.

Appendix C. Scale analysis

See Figs. C.10 and C.11.

Appendix D. Relationships between the clumping index derived from terrestrial laser scanning and the Sentinel-2 spectral bands

See Fig. D.12.

Appendix E. Relationships between the VV backscatter coefficient and VH/VV ratio derived from Sentinel-1 SAR data and the Sentinel-2 spectral bands

See Figs. E.13 and E.14.

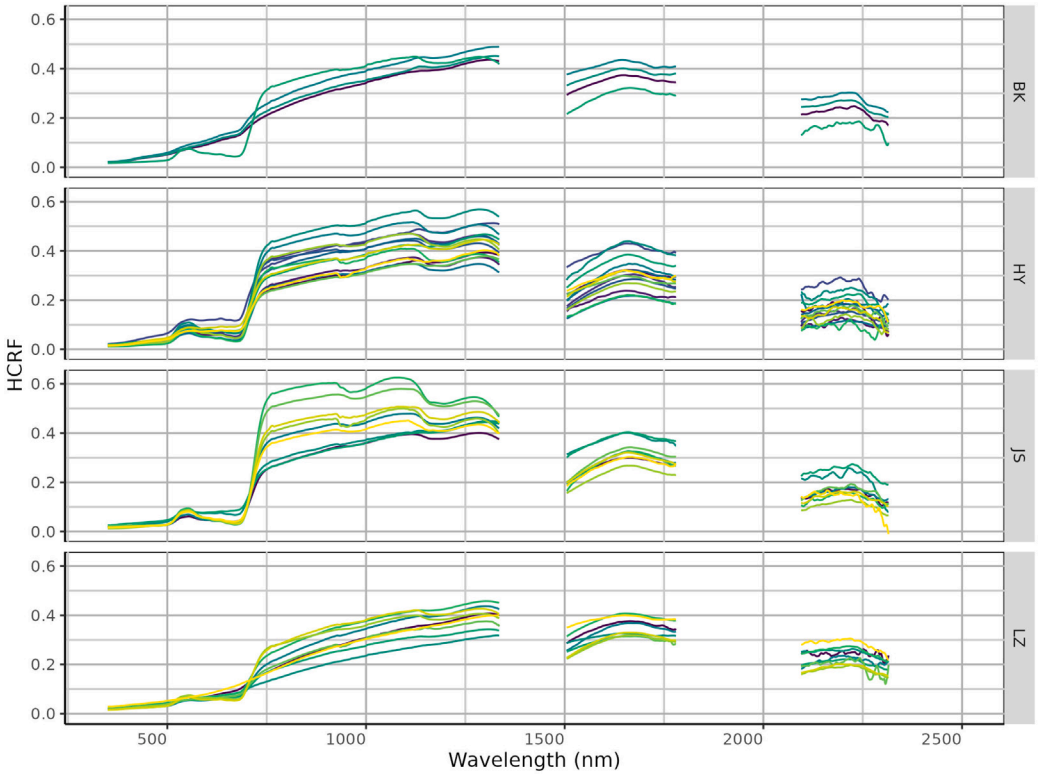

Fig. A.8. Mean spectral reflectance factors (HCRF, hemispherical-conical reflectance factors) of forest floor per stand in Hyytiälä (HY), Järvselja (JS), Bílý Kříž (BK) and Lanžhot (LZ).

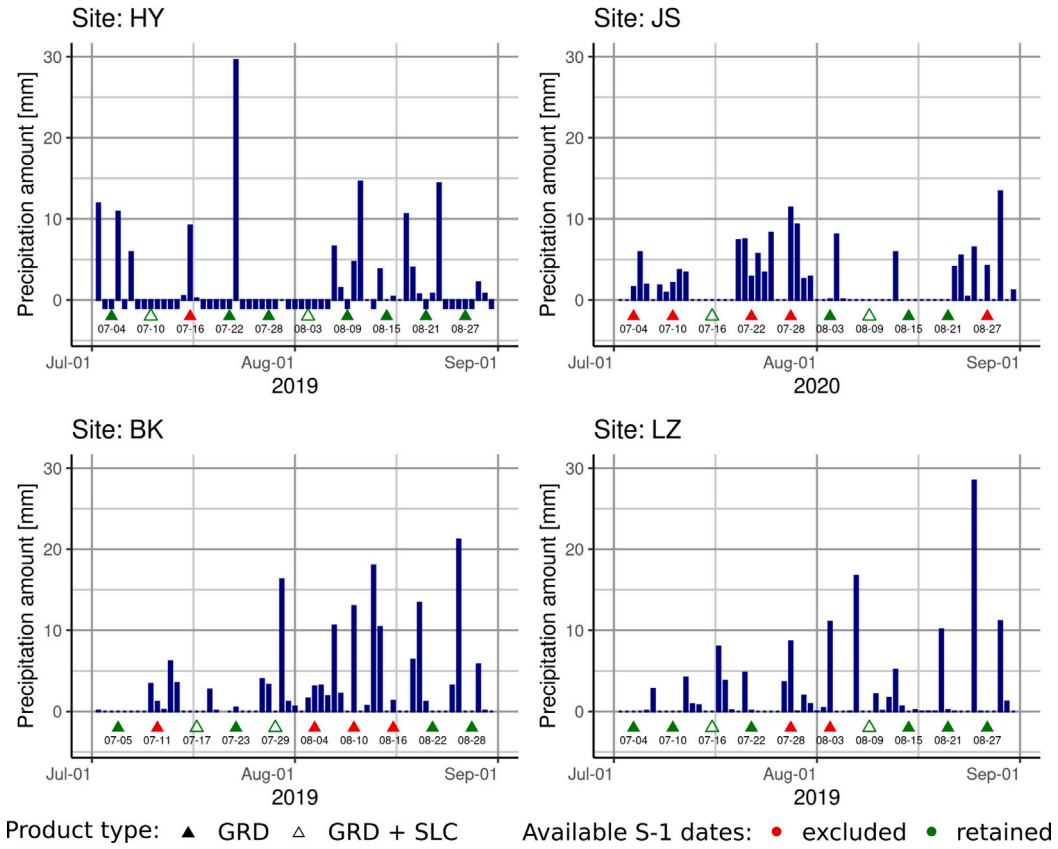

Fig. B.9. Dates of Sentinel-1 images available at the peak growing season (July–August) and daily precipitation in Hyytiälä (HY), Järvselja (JS), Bílý Kříž (BK) and Lanžhot (LZ). Sentinel-1 images excluded from the analysis due to daily precipitation higher than 1 mm are symbolized by the red triangles. The two SLC Sentinel-1 images downloaded to derive coherence appeared as green empty triangles. The GRD Sentinel-1 images used to derive backscatter coefficients correspond to green full and empty triangles. The meteorological measurements were conducted at the study areas, except for Järvselja where the weather station was about 50 km away (Tartu-Tõravere weather station). (For interpretation of the references to color in this figure legend, the reader is referred to the web version of this article.)

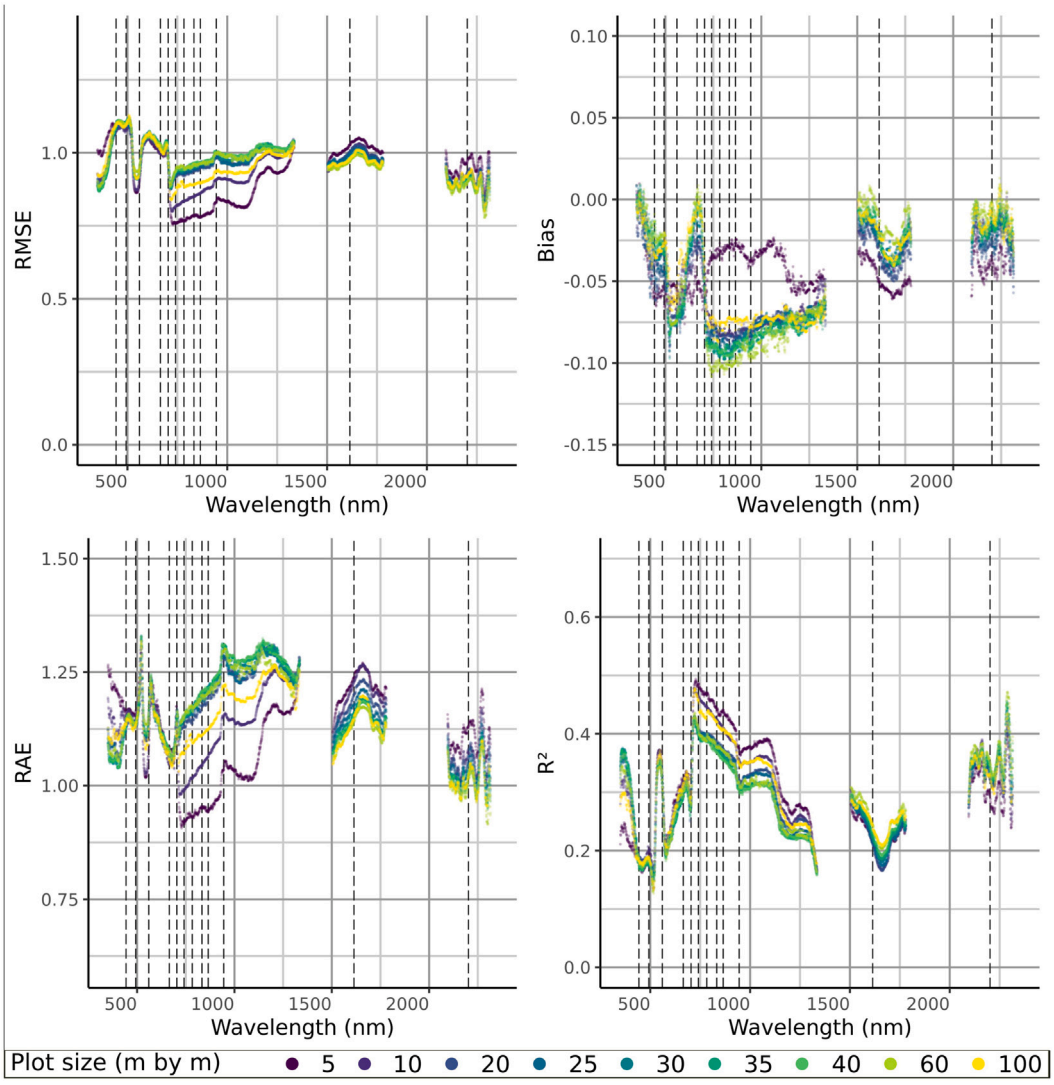

Fig. C.10. Average Root-Mean Square Error (RMSE), bias, Relative Absolute Error (RAE) and coefficient of determination (R^2) values computed for the ALS-derived metrics varying the plot size from 5 to 100 m. Vertical dashed lines indicate the wavelengths corresponding to the centers of the Sentinel-2 bands. We used a plot size of 25 m by 25 m (Fig. 3), because it provided the best models for predicting the full spectra within the range of plot sizes tested from 5 to 100 m.

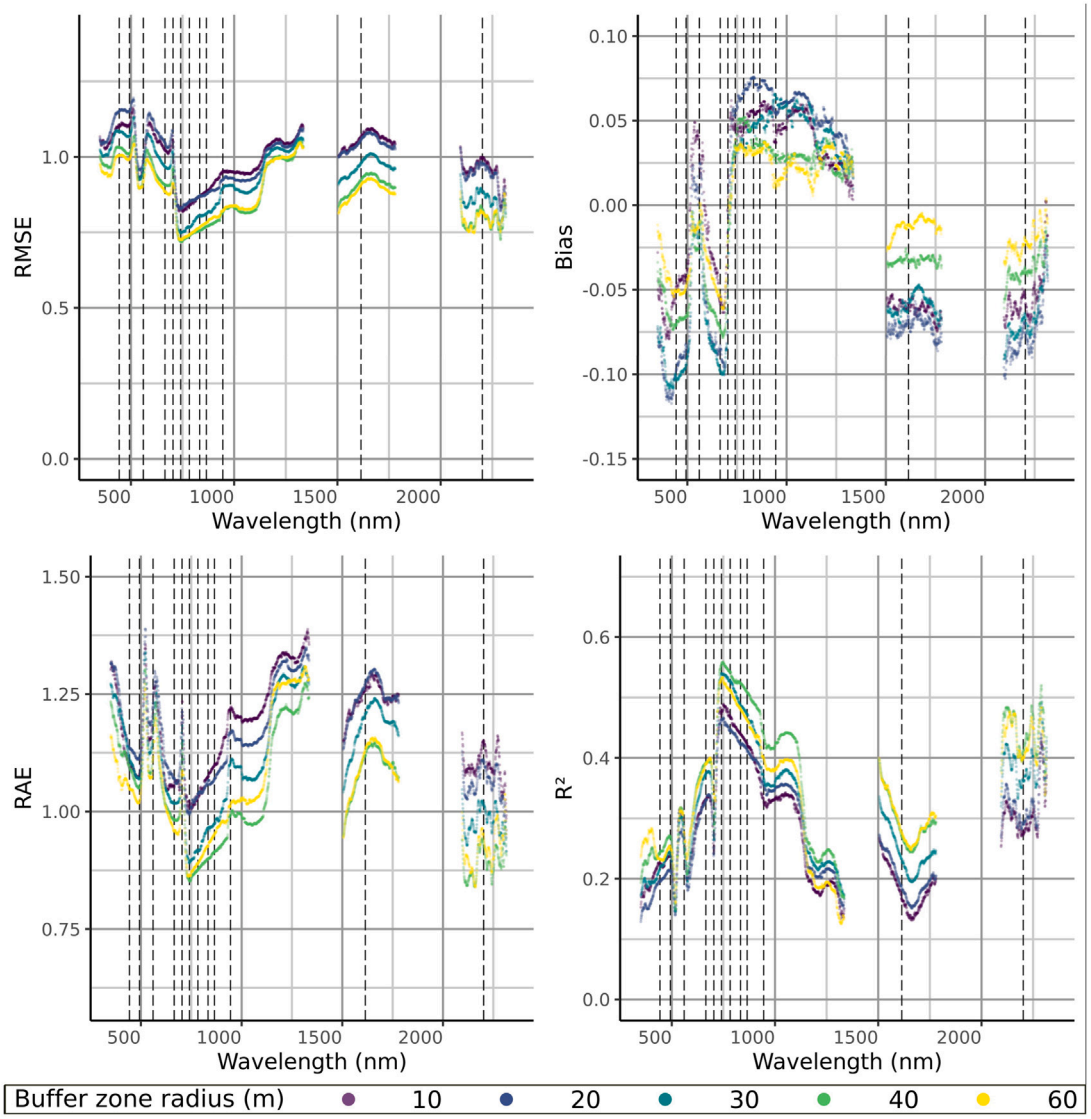

Fig. C.11. Average Root-Mean Square Error (RMSE), bias, Relative Absolute Error (RAE) and coefficient of determination (R^2) values computed for the SAR-derived metrics varying the buffer zone radius from 10 to 100 m. Vertical dashed lines indicate the wavelengths corresponding to the centers of the Sentinel-2 bands. We used a radius of 40 m (Fig. 3), because it provided the best models for predicting the full spectra within the range of radii tested from 10 to 100 m.

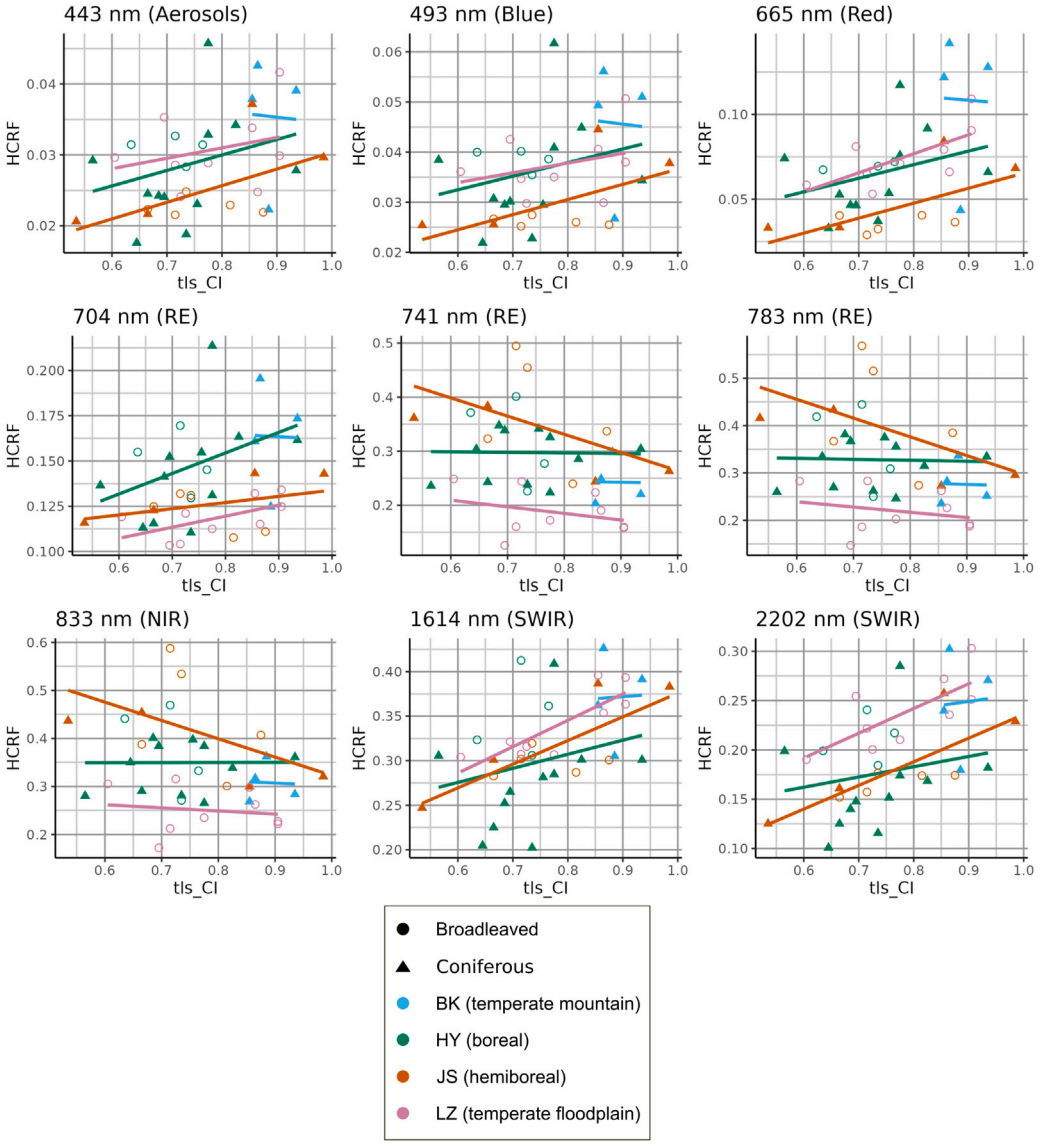

Fig. D.12. Relationships of forest structure metrics clumping index (CI) (from TLS) with hemispherical-conical reflectance factors (HCRF) of the forest floor (interval between 0 and 1) at different Sentinel-2 (S2) spectral bands. We show only those relationships demonstrated as potentially important by the Pearson correlation (p-value < 0.1). Linear regressions are represented by study areas, with Bílý Kříž, Hyytiälä, Järvselja and Lanžhot labeled BK, HY, JS and LZ. The forests dominated by broadleaved and coniferous trees are represented with circles and triangles, respectively.

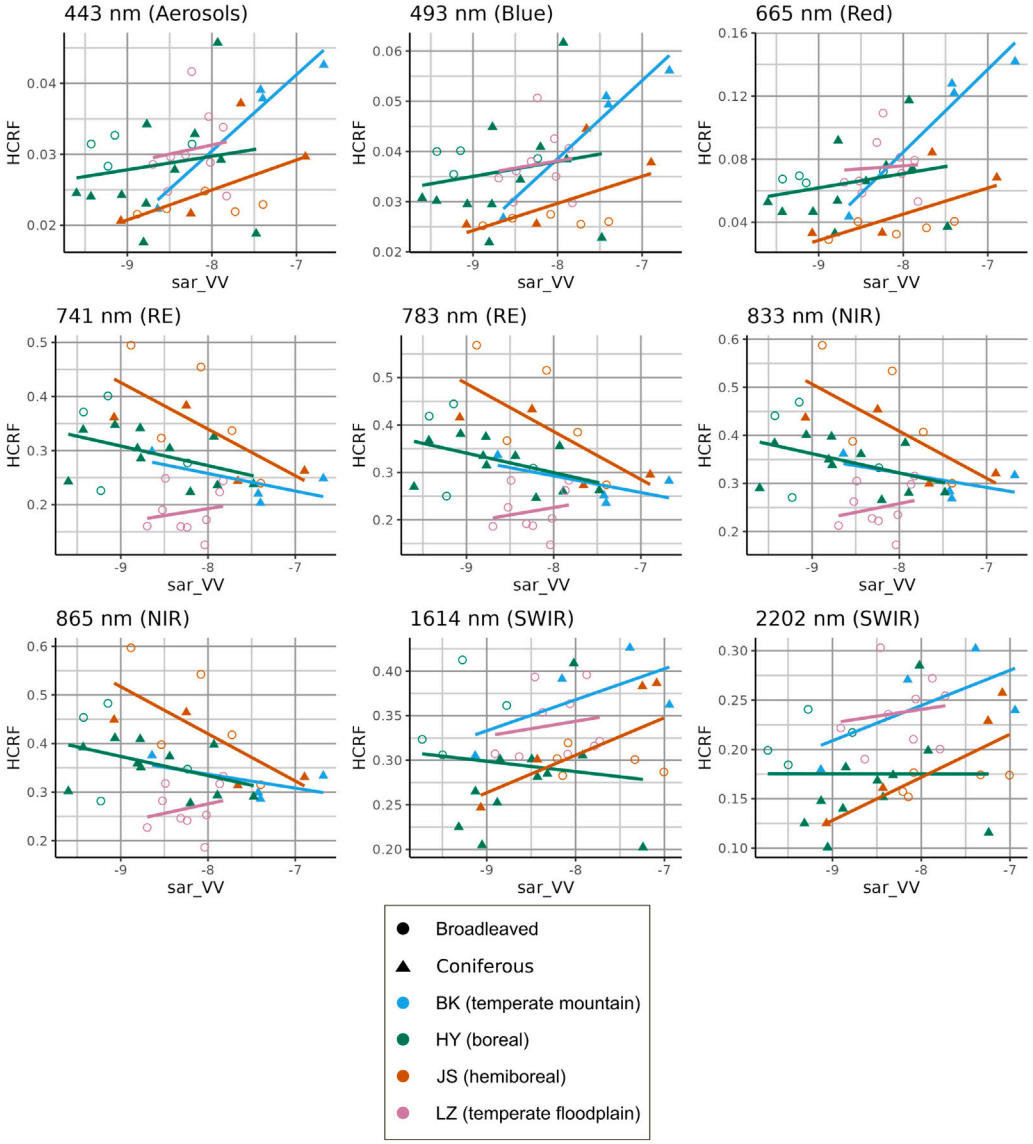

Fig. E.13. Relationships of forest structure metrics VV backscatter coefficient (from SAR) with hemispherical-conical reflectance factors (HCRF) of the forest floor (interval between 0 and 1) at different Sentinel-2 (S2) spectral bands. We show only those relationships demonstrated as potentially important by the Pearson correlation (p-value < 0.1). Linear regressions are represented by study areas, with Bílý Kříž, Hyytiälä, Järvselja and Lanžhot labeled BK, HY, JS and LZ. The forests dominated by broadleaved and coniferous trees are represented with circles and triangles, respectively.

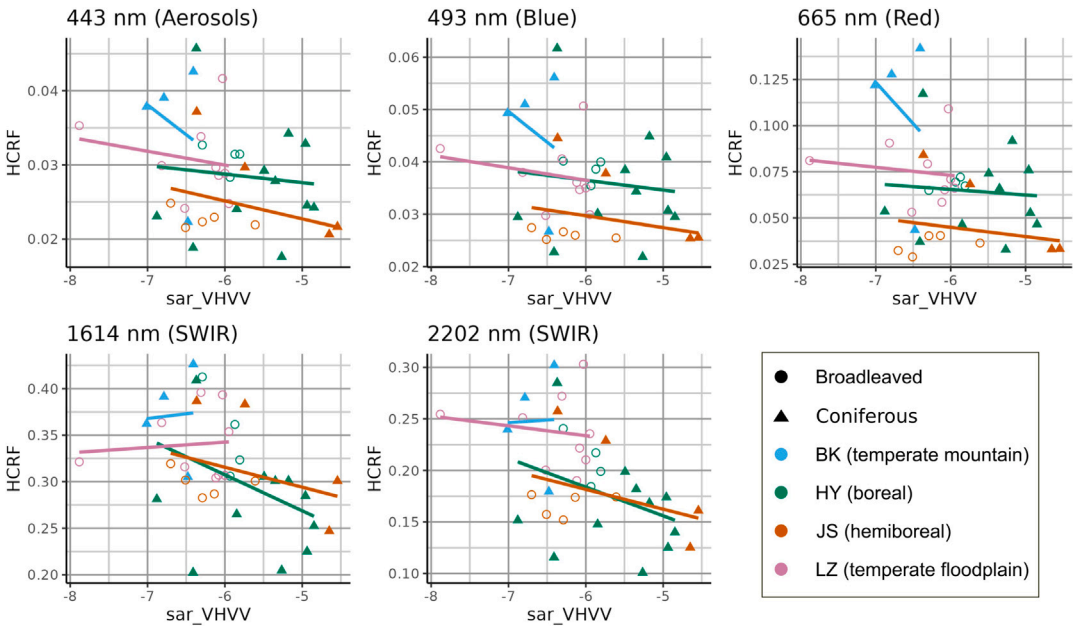

Fig. E.14. Relationships of forest structure metrics VH/VV ratio (from SAR) with hemispherical-conical reflectance factors (HCRF) of the forest floor (interval between 0 and 1) at different Sentinel-2 (S2) spectral bands. We show only those relationships demonstrated as potentially important by the Pearson correlation (p-value < 0.1). Linear regressions are represented by study areas, with Bílý Kříž, Hyytiälä, Järvselja and Lanžhot labeled BK, HY, JS and LZ. The forests dominated by broadleaved and coniferous trees are represented with circles and triangles, respectively.

Data availability

The field data are available from Hovi et al. (2024b) and the airborne laser scanning data from Hovi et al. (2024a). We also utilized Sentinel-1 data that is available from the Copernicus Data Space Ecosystem (Copernicus Data Space Ecosystem, 2023).

References

Acebes, P., Lillo, P., Jaime-González, C., 2021. Disentangling LiDAR contribution in modelling species–habitat structure relationships in terrestrial ecosystems worldwide. A systematic review and future directions. Remote Sens. 13 (17), 3447. http://dx.doi.org/10.3390/rs13173447, URL: https://www.mdpi.com/2072-4292/13/17/3447. Number: 17 Publisher: Multidisciplinary Digital Publishing Institute.

Alonso-Rego, C., Arellano-Pérez, S., Cabo, C., Ordoñez, C., Álvarez-González, J.G., Díaz-Varela, R.A., Ruiz-González, A.D., 2020. Estimating fuel loads and structural characteristics of shrub communities by using terrestrial laser scanning. Remote Sens. 12 (22), 3704. http://dx.doi.org/10.3390/rs12223704, URL: https://www.mdpi.com/2072-4292/12/22/3704. Number: 22 Publisher: Multidisciplinary Digital Publishing Institute.

Atwood, D.K., Small, D., Gens, R., 2012. Improving PolSAR land cover classification with radiometric correction of the coherency matrix. IEEE J. Sel. Top. Appl. Earth Obs. Remote Sens. 5 (3), 848–856. http://dx.doi.org/10.1109/JSTARS.2012.2186791, URL: https://ieeexplore.ieee.org/document/6186744. Conference Name: IEEE Journal of Selected Topics in Applied Earth Observations and Remote Sensing.

Barbier, S., Gosselin, F., Balandier, P., 2008. Influence of tree species on understory vegetation diversity and mechanisms involved—A critical review for temperate and boreal forests. Forest Ecol. Manag. 254 (1), 1–15. http://dx.doi.org/10.1016/j.foreco.2007.09.038, URL: https://www.sciencedirect.com/science/article/pii/S0378112707007025.

Bates, D., Mächler, M., Bolker, B., Walker, S., 2015. Fitting linear mixed-effects models using **lme4**. J. Stat. Softw. 67 (1), http://dx.doi.org/10.18637/jss.v067.i01, URL: http://www.jstatsoft.org/v67/i01/.

Borlaf-Mena, I., García-Duro, J., Santoro, M., Villard, L., Badea, O., Tanase, M.A., 2023. Seasonality and directionality effects on radar backscatter are key to identify mountain forest types with sentinel-1 data. Remote Sens. Environ. 296, 113728. http://dx.doi.org/10.1016/j.rse.2023.113728, URL: https://www.sciencedirect.com/science/article/pii/S0034425723002791.

Braziunas, K.H., Geres, L., Richter, T., Glasmann, F., Senf, C., Thom, D., Seibold, S., Seidl, R., 2024. Projected climate and canopy change lead to thermophilization and homogenization of forest floor vegetation in a hotspot of plant species richness. Global Change Biol. 30 (1), e17121. http://dx.doi.org/10.1111/gcb.17121, URL: https://onlinelibrary.wiley.com/doi/abs/10.1111/gcb.17121. _eprint: https://onlinelibrary.wiley.com/doi/pdf/10.1111/gcb.17121.

Bruggisser, M., Dorigo, W., Dostálová, A., Hollaus, M., Navacchi, C., Schlaffer, S., Pfeifer, N., 2021. Potential of sentinel-1 C-band time series to derive structural parameters of temperate deciduous forests. Remote Sens. 13 (4), 798. http://dx.doi.org/10.3390/rs13040798, URL: https://www.mdpi.com/2072-4292/13/4/798. Number: 4 Publisher: Multidisciplinary Digital Publishing Institute.

Canisius, F., Chen, J.M., 2007. Retrieving forest background reflectance in a boreal region from multi-angle imaging SpectroRadiometer (MISR) data. Remote Sens. Environ. 107 (1–2), 312–321. http://dx.doi.org/10.1016/j.rse.2006.07.023, URL: https://linkinghub.elsevier.com/retrieve/pii/S0034425706004184.

Copernicus Data Space Ecosystem, 2023. Copernicus data space ecosystem. URL: https://dataspace.copernicus.eu/.

De Frenne, P., 2023. Novel light regimes in European forests. Nat. Ecol. Evol. 1–7. http://dx.doi.org/10.1038/s41559-023-02242-2, URL: https://www.nature.com/articles/s41559-023-02242-2. Publisher: Nature Publishing Group.

De Frenne, P., Lenoir, J., Luoto, M., Scheffers, B.R., Zellweger, F., Aalto, J., Ashcroft, M.B., Christiansen, D.M., Decocq, G., De Pauw, K., Govaert, S., Greiser, C., Gril, E., Hampe, A., Jucker, T., Klinges, D.H., Koelemeijer, I.A., Lembrechts, J.J., Marrec, R., Meeussen, C., Ogée, J., Tyystjärvi, V., Vangansbeke, P., Hylander, K., 2021. Forest microclimates and climate change: Importance, drivers and future research agenda. Global Change Biol. 27 (11), 2279–2297. http://dx.doi.org/10.1111/gcb.15569, URL: https://onlinelibrary.wiley.com/doi/abs/10.1111/gcb.15569. _eprint: https://onlinelibrary.wiley.com/doi/pdf/10.1111/gcb.15569.

De Pauw, K., Sanczuk, P., Meeussen, C., Depauw, L., De Lombaerde, E., Govaert, S., Vanneste, T., Brunet, J., Cousins, S.A.O., Gasperini, C., Hedwall, P.-O., Iacopetti, G., Lenoir, J., Plue, J., Selvi, F., Spicher, F., Uria-Diez, J., Verheyen, K., Vangansbeke, P., De Frenne, P., 2022. Forest understorey communities respond strongly to light in interaction with forest structure, but not to microclimate warming. New Phytol. 233 (1), 219–235. http://dx.doi.org/10.1111/nph.17803, URL: https://onlinelibrary.wiley.com/doi/abs/10.1111/nph.17803. _eprint: https://onlinelibrary.wiley.com/doi/pdf/10.1111/nph.17803.

Di Stefano, F., Chiappini, S., Gorreja, A., Balestra, M., Pierdicca, R., 2021. Mobile 3D scan LiDAR: a literature review. Geomat. Natural Hazards Risk 12 (1), 2387–2429. http://dx.doi.org/10.1080/19475705.2021.1964617, Publisher: Taylor & Francis _eprint: https://doi.org/10.1080/19475705.2021.1964617.

Disney, M., 2019. Terrestrial LiDAR: a three-dimensional revolution in how we look at trees. New Phytol. 222 (4), 1736–1741. http://dx.doi.org/10.1111/nph.15517, URL: https://onlinelibrary.wiley.com/doi/abs/10.1111/nph.15517. _eprint: https://onlinelibrary.wiley.com/doi/pdf/10.1111/nph.15517.

Dostálová, A., Milenkovic, M., Hollaus, M., Wagner, W., 2016. Influence of forest structure on the Sentinel-1 backscatter variation - analysis with full-waveform lidar data. In: Living Planet Symposium. Vol. 740, p. 202.

Dostalova, A., Navacchi, C., Greimeister-Pfeil, I., Small, D., Wagner, W., 2022. The effects of radiometric terrain flattening on SAR-based forest mapping and classification. Remote Sens. Lett. 13 (9), 855–864. http://dx.doi.org/10.1080/2150704X.2022.2092911, Publisher: Taylor & Francis _eprint: https://doi.org/10.1080/2150704X.2022.2092911.

Eriksson, H.M., Eklundh, L., Kuusk, A., Nilson, T., 2006. Impact of understory vegetation on forest canopy reflectance and remotely sensed LAI estimates. Remote Sens. Environ. 103 (4), 408–418. http://dx.doi.org/10.1016/j.rse.2006.04.005, URL: https://www.sciencedirect.com/science/article/pii/S0034425706001556.

Fang, H., 2021. Canopy clumping index (CI): A review of methods, characteristics, and applications. Agricult. Forest. Meterol. 303, 108374. http://dx.doi.org/10.1016/j.agrformet.2021.108374, URL: https://www.sciencedirect.com/science/article/pii/S0168192321000575.

Fisher, R.A., Koven, C.D., 2020. Perspectives on the future of land surface models and the challenges of representing complex terrestrial systems. J. Adv. Modelling Earth Syst. 12 (4), e2018MS001453. http://dx.doi.org/10.1029/2018MS001453, URL: https://onlinelibrary.wiley.com/doi/abs/10.1029/2018MS001453. _eprint: https://onlinelibrary.wiley.com/doi/pdf/10.1029/2018MS001453.

Forsström, P.R., Hovi, A., Juola, J., Rautiainen, M., 2023. Links between light availability and spectral properties of forest floor in European forests. Agricult. Forest. Meterol. 336, 109481. http://dx.doi.org/10.1016/j.agrformet.2023.109481, URL: https://research.aalto.fi/en/publications/links-between-light-availability-and-spectral-properties-of-fores. Publisher: ELSEVIER SCIENCE B.V.

Forsström, P., Peltoniemi, J., Rautiainen, M., 2019. Seasonal dynamics of lingonberry and blueberry spectra. Silva Fennica 53 (2), http://dx.doi.org/10.14214/sf.10150, URL: https://www.silvafennica.fi/article/10150.

Ge, S., Tomppo, E., Rauste, Y., McRoberts, R.E., Praks, J., Gu, H., Su, W., Antropov, O., 2023. Sentinel-1 time series for predicting growing stock volume of boreal forest: Multitemporal analysis and feature selection. Remote Sens. 15 (14), 3489. http://dx.doi.org/10.3390/rs15143489, URL: https://www.mdpi.com/2072-4292/15/14/3489. Number: 14 Publisher: Multidisciplinary Digital Publishing Institute.

Geert, v.B., Laboissière, R., Wilhelm, H.D., 2021. Gsignal: Signal processing. URL: https://github.com/gjmvanboxtel/gsignal. original-date: 2019-11-20T14:44:11Z.

Goulden, M.L., Crill, P.M., 1997. Automated measurements of CO2 exchange at the moss surface of a black spruce forest. Tree Physiol. 17 (8–9), 537–542. http://dx.doi.org/10.1093/treephys/17.8-9.537.

Groll, A., 2023. glmmLasso: Variable selection for generalized linear mixed models by L1-penalized estimation. URL: https://cran.r-project.org/web/packages/glmmLasso/glmmLasso.pdf.

Guo, Q., Su, Y., Hu, T., Guan, H., Jin, S., Zhang, J., Zhao, X., Xu, K., Wei, D., Kelly, M., 2020. Lidar boosts 3D ecological observations and modelings: A review and perspective. IEEE Geosci. Remote Sens. Mag. 9 (1), 232–257. http://dx.doi.org/10.1109/MGRS.2020.3032713, Publisher: IEEE.

Hallik, L., Kull, O., Nilson, T., Peñuelas, J., 2009. Spectral reflectance of multispecies herbaceous and moss canopies in the boreal forest understory and open field. Can. J. Remote Sens. 35 (5), 474–485. http://dx.doi.org/10.5589/m09-040, Publisher: Taylor & Francis _eprint: https://doi.org/10.5589/m09-040.

Hancock, S., Essery, R., Reid, T., Carle, J., Baxter, R., Rutter, N., Huntley, B., 2014. Characterising forest gap fraction with terrestrial lidar and photography: An examination of relative limitations. Agricult. Forest. Meterol. 189–190, 105–114. http://dx.doi.org/10.1016/j.agrformet.2014.01.012, URL: https://www.sciencedirect.com/science/article/pii/S0168192314000215.

Hedwall, P.-O., Uria-Diez, J., Brunet, J., Gustafsson, L., Axelsson, A.-L., Strengbom, J., 2021. Interactions between local and global drivers determine long-term trends in boreal forest understorey vegetation. Global Ecol. Biogeogr. 30 (9), 1765–1780. http://dx.doi.org/10.1111/geb.13324, URL: https://onlinelibrary.wiley.com/doi/abs/10.1111/geb.13324. _eprint: https://onlinelibrary.wiley.com/doi/pdf/10.1111/geb.13324.

Herk, C.M.v., Aptroot, A., Dobben, H.F.v., 2002. Long-term monitoring in the Netherlands suggests that lichens respond to global warming. Lichenol. 34 (2), 141–154. http://dx.doi.org/10.1006/lich.2002.0378, URL: https://www.cambridge.org/core/journals/lichenologist/article/abs/longterm-monitoring-in-the-netherlands-suggests-that-lichens-respond-to-global-warming/CB7851EBCDD8BF8BCA991A91E237F5A3. Publisher: Cambridge University Press.

Hoffmann, J., Muro, J., Dubovyk, O., 2022. Predicting species and structural diversity of temperate forests with satellite remote sensing and deep learning. Remote Sens. 14 (7), 1631. http://dx.doi.org/10.3390/rs14071631, URL: https://www.mdpi.com/2072-4292/14/7/1631. Number: 7 Publisher: Multidisciplinary Digital Publishing Institute.

Holzwarth, S., Thonfeld, F., Abdullahi, S., Asam, S., Da Ponte Canova, E., Gessner, U., Huth, J., Kraus, T., Leutner, B., Kuenzer, C., 2020. Earth observation based monitoring of forests in Germany: A review. Remote Sens. 12 (21), 3570. http://dx.doi.org/10.3390/rs12213570, URL: https://www.mdpi.com/2072-4292/12/21/3570. Number: 21 Publisher: Multidisciplinary Digital Publishing Institute.

Hovi, A., Schraik, D., Hanuš, J., Homolová, L., Juola, J., Lang, M., Lukeš, P., Pisek, J., Rautiainen, M., 2022. Assessment of a photon recollision probability based forest reflectance model in European boreal and temperate forests. Remote Sens. Environ. 269, 112804. http://dx.doi.org/10.1016/j.rse.2021.112804, URL: https://www.sciencedirect.com/science/article/pii/S0034425721005241.

Hovi, A., Schraik, D., Hanuš, J., Lukeš, P., Lhotáková, Z., Homolová, L., Rautiainen, M., 2024a. A Spectral-Structural Characterization of European Temperate, Hemiboreal and Boreal Forests: Airborne Data. Aalto University, https://doi.org/10.23729/c6da63dd-f527-4ec9-8401-57c14f77d19f.

Hovi, A., Schraik, D., Hanuš, J., Lukeš, P., Lhotáková, Z., Homolová, L., Rautiainen, M., 2024b. A Spectral-Structural Characterization of European Temperate, Hemiboreal and Boreal Forests: Laboratory and Field Data. Aalto University, https://doi.org/10.23729/9a8d90cd-73e2-438d-9230-94e10e61adc9.

Hovi, A., Schraik, D., Kuusinen, N., Fabiánek, T., Hanuš, J., Homolová, L., Juola, J., Lukeš, P., Rautiainen, M., 2023. Synergistic use of multi- and hyperspectral remote sensing data and airborne LiDAR to retrieve forest floor reflectance. Remote Sens. Environ. 293, 113610. http://dx.doi.org/10.1016/j.rse.2023.113610, URL: https://www.sciencedirect.com/science/article/pii/S003442572300161X.

Joshi, N., Mitchard, E.T.A., Brolly, M., Schumacher, J., Fernández-Landa, A., Johannsen, V.K., Marchamalo, M., Fensholt, R., 2017. Understanding 'saturation' of radar signals over forests. Sci. Rep. 7 (1), 3505. http://dx.doi.org/10.1038/s41598-017-03469-3, URL: https://www.nature.com/articles/s41598-017-03469-3.

Juola, J., Rautiainen, M., 2022. A dataset of stem reflectance spectra for standing dead Scots pine trees. http://dx.doi.org/10.17632/8dvx3vvvk9.1, 1. URL: https://data.mendeley.com/datasets/8dvx3vvvk9/1. Publisher: Mendeley Data.

Koelemeijer, I.A., Ehrlén, J., De Frenne, P., Jönsson, M., Berg, P., Hylander, K., 2023. Forest edge effects on moss growth are amplified by drought. Ecol. Appl. 33 (4), e2851. http://dx.doi.org/10.1002/eap.2851, URL: https://onlinelibrary.wiley.com/doi/abs/10.1002/eap.2851. _eprint: https://onlinelibrary.wiley.com/doi/pdf/10.1002/eap.2851.

Kolari, P., Pumpanen, J., Kulmala, L., Ilvesniemi, H., Nikinmaa, E., Grönholm, T., Hari, P., 2006. Forest floor vegetation plays an important role in photosynthetic production of boreal forests. Forest Ecol. Manag. 221 (1), 241–248. http://dx.doi.org/10.1016/j.foreco.2005.10.021, URL: https://www.sciencedirect.com/science/article/pii/S0378112705005876.

Kuusinen, N., Hovi, A., Rautiainen, M., 2023. Estimation of boreal forest floor lichen cover using hyperspectral airborne and field data. Silva Fennica 57 (1), http://dx.doi.org/10.14214/sf.22014, URL: https://www.silvafennica.fi/article/22014.

Kuusinen, N., Juola, J., Karki, B., Stenroos, S., Rautiainen, M., 2020. A spectral analysis of common boreal ground lichen species. Remote Sens. Environ. 247, 111955. http://dx.doi.org/10.1016/j.rse.2020.111955, URL: https://www.sciencedirect.com/science/article/pii/S0034425720303254.

Labenski, P., Ewald, M., Schmidtlein, S., Heinsch, F.A., Fassnacht, F.E., 2023. Quantifying surface fuels for fire modelling in temperate forests using airborne lidar and sentinel-2: potential and limitations. Remote Sens. Environ. 295, 113711. http://dx.doi.org/10.1016/j.rse.2023.113711, URL: https://www.sciencedirect.com/science/article/pii/S0034425723002626.

Le Toan, T., Beaudoin, A., Riom, J., Guyon, D., 1992. Relating forest biomass to SAR data. IEEE Trans. Geosci. Remote Sens. 30 (2), 403–411. http://dx.doi.org/10.1109/36.134089, URL: https://ieeexplore.ieee.org/abstract/document/134089. Conference Name: IEEE Transactions on Geoscience and Remote Sensing.

Li, X., Liu, Y., Xu, W., Huang, P., Fu, W., 2019. Forest canopy volume density index inversion method using polarization decomposition. In: 2019 Photonics & Electromagnetics Research Symposium - Fall. PIERS - Fall, pp. 3063–3070. http://dx.doi.org/10.1109/PIERS-Fall48861.2019.9021425, URL: https://ieeexplore.ieee.org/document/9021425.

Majasalmi, T., Rautiainen, M., 2020. The impact of tree canopy structure on understory variation in a boreal forest. Forest Ecol. Manag. 466, 118100. http://dx.doi.org/10.1016/j.foreco.2020.118100, URL: https://www.sciencedirect.com/science/article/pii/S0378112720300372.

Manninen, T., 2012. High resolution boreal forest LAI maps using dual polarization SAR images. In: 2012 IEEE International Geoscience and Remote Sensing Symposium. IEEE, Munich, Germany, pp. 1680–1683. http://dx.doi.org/10.1109/IGARSS.2012.6351203, URL: http://ieeexplore.ieee.org/document/6351203/.

Markiet, V., Mõttus, M., 2020. Estimation of boreal forest floor reflectance from airborne hyperspectral data of coniferous forests. Remote Sens. Environ. 249, 112018. http://dx.doi.org/10.1016/j.rse.2020.112018, URL: https://www.sciencedirect.com/science/article/pii/S0034425720303886.

Mercier, A., Karlqvist, S., Hovi, A., Rautiainen, M., 2023. Reflectance spectra of boreal forest floor elements: ferns, herbaceous plants and decaying wood. http://dx.doi.org/10.17632/dddb2prk4p.1, 1. URL: https://data.mendeley.com/datasets/dddb2prk4p/1. Publisher: Mendeley Data.

Messier, C., Doucet, R., Ruel, J.-C., Claveau, Y., Kelly, C., Lechowicz, M.J., 1999. Functional ecology of advance regeneration in relation to light in boreal forests. Can. J. Forest Res. 29 (6), 812–823. http://dx.doi.org/10.1139/x99-070, URL: https://cdnsciencepub.com/doi/abs/10.1139/x99-070. Publisher: NRC Research Press.

Morén, A.-S., Lindroth, A., 2000. CO2 exchange at the floor of a boreal forest. Agricult. Forest. Meterol. 101 (1), 1–14. http://dx.doi.org/10.1016/S0168-1923(99)00160-4, URL: https://www.sciencedirect.com/science/article/pii/S0168192399001604.

Mõttus, M., Dees, M., Astola, H., Dałek, S., Halme, E., Häme, T., Krzyżanowska, M., Mäkelä, A., Marin, G., Minunno, F., Pawlowski, G., Penttilä, J., Rasinmäki, J., 2021. A methodology for implementing a digital twin of the earth's forests to match the requirements of different user groups. GI_Forum 1, 130–136. http://dx.doi.org/10.1553/giscience2021_01_s130, URL: https://hw.oeaw.ac.at?arp=0x003c9b66.

Mulatu, K.A., Decuyper, M., Brede, B., Kooistra, L., Reiche, J., Mora, B., Herold, M., 2019. Linking terrestrial LiDAR scanner and conventional forest structure measurements with multi-modal satellite data. Forests 10 (3), 291. http://dx.doi.org/10.3390/f10030291, URL: https://www.mdpi.com/1999-4907/10/3/291. Number: 3 Publisher: Multidisciplinary Digital Publishing Institute.

Næsset, E., 2002. Predicting forest stand characteristics with airborne scanning laser using a practical two-stage procedure and field data. Remote Sens. Environ. 80 (1), 88–99. http://dx.doi.org/10.1016/S0034-4257(01)00290-5, URL: https://www.sciencedirect.com/science/article/pii/S0034425701002905.

Nikopensius, M., Pisek, J., Raabe, K., 2015. Spectral reflectance patterns and seasonal dynamics of common understory types in three mature hemi-boreal forests. Int. J. Appl. Earth Obs. Geoinf. 43, 84–91. http://dx.doi.org/10.1016/j.jag.2014.11.012, URL: https://www.sciencedirect.com/science/article/pii/S0303243414002621.

Pimont, F., Allard, D., Soma, M., Dupuy, J.-L., 2018. Estimators and confidence intervals for plant area density at voxel scale with T-lidar. Remote Sens. Environ. 215, 343–370. http://dx.doi.org/10.1016/j.rse.2018.06.024, URL: https://www.sciencedirect.com/science/article/pii/S003442571830302X.

Pisek, J., Erb, A., Korhonen, L., Biermann, T., Carrara, A., Cremonese, E., Cuntz, M., Fares, S., Gerosa, G., Grünwald, T., Hase, N., Heliasz, M., Ibrom, A., Knohl, A., Kobler, J., Kruijt, B., Lange, H., Leppänen, L., Limousin, J.-M., Serrano, F.R.L., Loustau, D., Lukeš, P., Lundin, L., Marzuoli, R., Mölder, M., Montagnani, L., Neirynck, J., Peichl, M., Rebmann, C., Rubio, E., Santos-Reis, M., Schaaf, C., Schmidt, M., Simioni, G., Soudani, K., Vincke, C., 2021. Retrieval and validation of forest background reflectivity from daily moderate resolution imaging spectroradiometer (MODIS) bidirectional reflectance distribution function (BRDF) data across European forests. Biogeosciences 18 (2), 621–635. http://dx.doi.org/10.5194/bg-18-621-2021, URL: https://bg.copernicus.org/articles/18/621/2021/. Publisher: Copernicus GmbH.

Pisek, J., Rautiainen, M., Heiskanen, J., Mõttus, M., 2012. Retrieval of seasonal dynamics of forest understory reflectance in a northern European boreal forest from MODIS BRDF data. Remote Sens. Environ. 117, 464–468. http://dx.doi.org/10.1016/j.rse.2011.09.012, URL: https://www.sciencedirect.com/science/article/pii/S0034425711003397.

R Core Team, 2023. R: A language and environment for statistical computing. URL: https://www.R-project.org/.

Rantala, S., Pekkinen, E., Tammiruusu, S. (Eds.), 2011. Finnish Forestry Practice and Management. Metsäkustannus, Helsinki.

Rautiainen, M., Heiskanen, J., 2013. Seasonal contribution of understory vegetation to the reflectance of a boreal landscape at different spatial scales. IEEE Geosci. Remote Sens. Lett. 10 (4), 923–927. http://dx.doi.org/10.1109/LGRS.2013.2247560, URL: https://ieeexplore.ieee.org/abstract/document/6484882. Conference Name: IEEE Geoscience and Remote Sensing Letters.

Rautiainen, M., Mõttus, M., Heiskanen, J., Akujärvi, A., Majasalmi, T., Stenberg, P., 2011. Seasonal reflectance dynamics of common understory types in a northern European boreal forest. Remote Sens. Environ. 115 (12), 3020–3028. http://dx.doi.org/10.1016/j.rse.2011.06.005, URL: https://www.sciencedirect.com/science/article/pii/S003442571100229X.

Rautiainen, M., Stenberg, P., 2005. Application of photon recollision probability in coniferous canopy reflectance simulations. Remote Sens. Environ. 96 (1), 98–107. http://dx.doi.org/10.1016/j.rse.2005.02.009, URL: https://www.sciencedirect.com/science/article/pii/S0034425705000908.

Rocchini, D., Foody, G.M., Nagendra, H., Ricotta, C., Anand, M., He, K.S., Amici, V., Kleinschmit, B., Förster, M., Schmidtlein, S., Feilhauer, H., Ghisla, A., Metz, M., Neteler, M., 2013. Uncertainty in ecosystem mapping by remote sensing. Comput. Geosci. 50, 128–135. http://dx.doi.org/10.1016/j.cageo.2012.05.022, URL: https://www.sciencedirect.com/science/article/pii/S0098300412001781.

Rosenqvist, A., Jones, C.E., Rignot, E., Simons, M., Siqueira, P., Tadono, T., 2021. A review of SAR observation requirements for global and targeted science applications. In: 2021 IEEE International Geoscience and Remote Sensing Symposium IGARSS. pp. 1745–1748. http://dx.doi.org/10.1109/IGARSS47720.2021.9553966, URL: https://ieeexplore.ieee.org/abstract/document/9553966. ISSN: 2153-7003.

Salko, S.-S., Juola, J., Burdun, I., Vasander, H., Rautiainen, M., 2023. Intra- and interspecific variation in spectral properties of dominant Sphagnum moss species in boreal peatlands. Ecol. Evol. 13 (6), e10197. http://dx.doi.org/10.1002/ece3.10197, URL: https://onlinelibrary.wiley.com/doi/abs/10.1002/ece3.10197. _eprint: https://onlinelibrary.wiley.com/doi/pdf/10.1002/ece3.10197.

Santoro, M., Cartus, O., Fransson, J.E.S., Wegmüller, U., 2019. Complementarity of X-, C-, and L-band SAR backscatter observations to retrieve forest stem volume in boreal forest. Remote Sens. 11 (13), 1563. http://dx.doi.org/10.3390/rs11131563, URL: https://www.mdpi.com/2072-4292/11/13/1563. Number: 13 Publisher: Multidisciplinary Digital Publishing Institute.

Schraik, D., Wang, D., Hovi, A., Rautiainen, M., 2023. Quantifying stand-level clumping of boreal, hemiboreal and temperate European forest stands using terrestrial laser scanning. Agricult. Forest. Meterol. 339, 109564. http://dx.doi.org/10.1016/j.agrformet.2023.109564, URL: https://www.sciencedirect.com/science/article/pii/S0168192323002551.

Sentinel-2 MSI Technical Guide, 2024. MSI instrument – sentinel-2 MSI technical guide – sentinel online. URL: https://copernicus.eu/technical-guides/sentinel-2-msi/msi-instrument.

SentiWiki, 2024. S1 mission. URL: https://sentiwiki.copernicus.eu/web/s1-mission.

Stefanidou, A., Z. Gitas, I., Korhonen, L., Georgopoulos, N., Stavrakoudis, D., 2020. Multispectral LiDAR-based estimation of surface fuel load in a dense coniferous forest. Remote Sens. 12 (20), 3333. http://dx.doi.org/10.3390/rs12203333, URL: https://www.mdpi.com/2072-4292/12/20/3333. Number: 20 Publisher: Multidisciplinary Digital Publishing Institute.

Su, Y., Guo, Q., Fry, D.L., Collins, B.M., Kelly, M., Flanagan, J.P., Battles, J.J., 2016. A vegetation mapping strategy for conifer forests by combining airborne LiDAR data and aerial imagery. Can. J. Remote Sens. 42 (1), 1–15. http://dx.doi.org/10.1080/07038992.2016.1131114, Publisher: Taylor & Francis _eprint: https://doi.org/10.1080/07038992.2016.1131114.

Tibshirani, R., 1996. Regression shrinkage and selection via the lasso. J. R. Stat. Soc. Ser. B Stat. Methodol. 58 (1), 267–288. http://dx.doi.org/10.1111/j.2517-6161.1996.tb02080.x, URL: https://rss.onlinelibrary.wiley.com/doi/10.1111/j.2517-6161.1996.tb02080.x.

Tredennick, A.T., Hooker, G., Ellner, S.P., Adler, P.B., 2021. A practical guide to selecting models for exploration, inference, and prediction in ecology. Ecology 102 (6), http://dx.doi.org/10.1002/ecy.3336, URL: https://onlinelibrary.wiley.com/doi/10.1002/ecy.3336.

Varhola, A., Frazer, G.W., Teti, P., Coops, N.C., 2012. Estimation of forest structure metrics relevant to hydrologic modelling using coordinate transformation of airborne laser scanning data. Hydrol. Earth Syst. Sci. 16 (10), 3749–3766. http://dx.doi.org/10.5194/hess-16-3749-2012, URL: https://hess.copernicus.org/articles/16/3749/2012/. Publisher: Copernicus GmbH.

Wang, D., 2024. leWoS. URL: https://github.com/dwang520/LeWoS. original-date: 2019-08-16T19:43:50Z.

Wang, D., Liang, X., Mofack, G.I., Martin-Ducup, O., 2021. Individual tree extraction from terrestrial laser scanning data via graph pathing. Forest Ecosyst. 8, 67. http://dx.doi.org/10.1186/s40663-021-00340-w, URL: https://www.sciencedirect.com/science/article/pii/S2197562023000386.

Wang, D., Momo Takoudjou, S., Casella, E., 2020. LeWoS: A universal leaf-wood classification method to facilitate the 3D modelling of large tropical trees using terrestrial LiDAR. Methods Ecol. Evol. 11 (3), 376–389. http://dx.doi.org/10.1111/2041-210X.13342, URL: https://onlinelibrary.wiley.com/doi/abs/10.1111/2041-210X.13342. _eprint: https://onlinelibrary.wiley.com/doi/pdf/10.1111/2041-210X.13342.

Webster, C., Mazzotti, G., Essery, R., Jonas, T., 2020. Enhancing airborne LiDAR data for improved forest structure representation in shortwave transmission models. Remote Sens. Environ. 249, 112017. http://dx.doi.org/10.1016/j.rse.2020.112017, URL: https://www.sciencedirect.com/science/article/pii/S0034425720303874.

Westman, W.E., Paris, J.F., 1987. Detecting forest structure and biomass with C-band multipolarization radar: Physical model and field tests. Remote Sens. Environ. 22 (2), 249–269. http://dx.doi.org/10.1016/0034-4257(87)90061-7, URL: https://linkinghub.elsevier.com/retrieve/pii/0034425787900617.

Xu, R., Li, Y., Teuling, A.J., Zhao, L., Spracklen, D.V., Garcia-Carreras, L., Meier, R., Chen, L., Zheng, Y., Lin, H., Fu, B., 2022. Contrasting impacts of forests on cloud cover based on satellite observations. Nature Commun. 13 (1), 670. http://dx.doi.org/10.1038/s41467-022-28161-7, URL: https://www.nature.com/articles/s41467-022-28161-7. Publisher: Nature Publishing Group.

Zahidi, I., Yusuf, B., Hamedianfar, A., Shafri, H.Z.M., Mohamed, T.A., 2015. Object-based classification of QuickBird image and low point density LIDAR for tropical trees and shrubs mapping. Eur. J. Remote Sens. 48 (1), 423–446. http://dx.doi.org/10.5721/EuJRS20154824, Publisher: Taylor & Francis _eprint: https://doi.org/10.5721/EuJRS20154824.

Zellweger, F., Baltensweiler, A., Schleppi, P., Huber, M., Küchler, M., Ginzler, C., Jonas, T., 2019. Estimating below-canopy light regimes using airborne laser scanning: An application to plant community analysis. Ecol. Evol. 9 (16), 9149–9159. http://dx.doi.org/10.1002/ece3.5462, URL: https://onlinelibrary.wiley.com/doi/abs/10.1002/ece3.5462. _eprint: https://onlinelibrary.wiley.com/doi/pdf/10.1002/ece3.5462.